Mesoscale Circulations

Earlier chapters focused primarily on the dynamics of synoptic- and planetary-scale circulations. Such large-scale motions are strongly influenced by the rotation of Earth so that outside the equatorial zone the Coriolis force dominates over inertia (i.e., the Rossby number is small). To first approximation, large-scale motions can be modeled by quasi-geostrophic theory (as shown in Chapter 6).

The study of quasi-geostrophic motions has been a central theme of dynamic meteorology for many years. Not all important circulations fit into the quasi-geostrophic classification, however. Some have Rossby numbers of order unity, and some are hardly influenced by Earth's rotation at all. Such circulations include a wide variety of phenomena. They all, however, are characterized by horizontal scales that are smaller than the synoptic scale (i.e., the *macroscale* of motion) but larger than the scale of an individual fair-weather cumulus cloud (i.e., the *microscale*). Hence, they can be classified conveniently as *mesoscale* circulations. Most severe weather is associated with mesoscale motion systems. Thus, understanding of the mesoscale is of both scientific and practical importance.

9.1 ENERGY SOURCES FOR MESOSCALE CIRCULATIONS

Mesoscale dynamics is generally defined to include the study of motion systems that have horizontal scales in the range of about 10 to 1000 km. It includes circulations ranging from thunderstorms and internal gravity waves at the small end of the scale to fronts and hurricanes at the large end. Given the diverse nature of mesoscale systems, it is not surprising that there is no single conceptual framework equivalent to the quasi-geostrophic theory that can provide a unified model for the dynamics of the mesoscale. Indeed, the dominant dynamical processes vary enormously depending on the type of mesoscale circulation system involved.

Possible sources of mesoscale disturbances include instabilities that occur intrinsically on the mesoscale, forcing by mesoscale thermal or topographic sources, nonlinear transfer of energy from either macroscale or microscale motions, and interaction of cloud physical and dynamical processes.

Although instabilities associated with the mean velocity or thermal structure of the atmosphere are a rich source of atmospheric disturbances, most instabilities have their maximum growth rates either on the large scale (baroclinic and most barotropic instability) or on the small scale (convection and Kelvin–Helmholtz instability). Only symmetric instability (to be discussed in Section 9.3) appears to be an intrinsically mesoscale instability.

Mountain waves created by flow over the individual peaks are generally regarded as small-scale phenomena. However, flow over large mountain ranges can produce orographic disturbances in the 10- to 100-km mesoscale range, whose characteristics depend on the mean wind and static stability profiles and the scale of the orography. Flow over mountain ranges, such as the Front Range of the Colorado Rockies, can under some conditions of mean flow and static stability lead to strong downslope wind storms.

Energy transfer from small scales to the mesoscale is a primary energy source for mesoscale convective systems. These may start as individual convective cells, which grow and combine to form thunderstorms; convective complexes such as squall lines and mesocyclones; and even hurricanes. Conversely, energy transfer from the large scale associated with temperature and vorticity advection in synoptic-scale circulations is responsible for the development of frontal circulations.

9.2 FRONTS AND FRONTOGENESIS

In the discussion of baroclinic instability in Chapter 7, the mean thermal wind U_T was taken to be a constant independent of the y coordinate. That assumption was necessary to obtain a mathematically simple model that retained the basic instability mechanism. It was pointed out in Section 6.1, however, that baroclinicity is not distributed uniformly in the atmosphere. Rather, horizontal temperature gradients tend to be concentrated in baroclinic zones associated with tropospheric jet streams. Not surprisingly, the development of baroclinic waves is also concentrated in such regions.

We showed in Chapter 7 that the energetics of baroclinic waves require that they remove available potential energy from the mean flow. Thus, on average baroclinic wave development tends to weaken the meridional temperature gradient (i.e., reduce the mean thermal wind). The mean pole-to-equator temperature gradient is of course restored continually by differential solar heating, which maintains the time-averaged temperature gradient pattern. In addition, there are transient dynamical processes that produce zones with greatly enhanced temperature gradients within individual baroclinic eddies. Such zones, which are particularly intense at the surface, are referred to as *fronts*.

Processes that generate fronts are called *frontogenetic*. Frontogenesis usually occurs in association with developing baroclinic waves, which in turn are concentrated in the storm tracks associated with the time-mean jetstreams. Thus,

even though on average baroclinic disturbances transport heat down the mean temperature gradient and tend to weaken the temperature difference between the polar and tropical regions, locally the flow associated with baroclinic disturbances may actually enhance the temperature gradient.

9.2.1 The Kinematics of Frontogenesis

A complete discussion of the dynamics of frontogenesis is beyond the scope of this text. A qualitative description of frontogenesis can be obtained, however, by considering the evolution of the temperature gradient when temperature is treated as a passive tracer in a specified horizontal flow field. Such an approach is referred to as *kinematic*; it considers the effects of advection on a field variable without reference to the underlying physical forces or to any influence of the advected tracer on the flow field.

The influence of a purely geostrophic flow on the temperature gradient was given in terms of the **Q** vector in (6.51). If for simplicity we focus on the meridional temperature gradient, then from (6.46) neglecting ageostrophic and diabatic effects gives

$$\frac{D_g}{Dt}\left(\frac{\partial T}{\partial y}\right) = -\left[\frac{\partial u_g}{\partial y}\frac{\partial T}{\partial x} - \frac{\partial u_g}{\partial x}\frac{\partial T}{\partial y}\right] \tag{9.1}$$

where we have used the fact that the geostrophic wind is nondivergent so that $\partial v_g/\partial y = -\partial u_g/\partial x$. The two terms within the brackets on the right in (9.1) can be interpreted as the forcing of the meridional temperature gradient by horizontal shear deformation and stretching deformation, respectively.

Horizontal shear has two effects on a fluid parcel: It tends to rotate the parcel (due to shear vorticity) and to deform the parcel through stretching parallel to the shear vector (i.e., along the x axis in Figure 9.1a) and shrinking along the horizontal direction perpendicular to the shear vector. Thus, the x-directed temperature gradient in Figure 9.1a is both rotated into the positive y direction and intensified by the shear. Horizontal shear is an important frontogenetic mechanism in both cold and warm fronts. For example, in the schematic surface pressure chart of Figure 9.2, the geostrophic wind has a northerly component west of point B and a southerly component east of point B. The resulting cyclonic shear will tend to rotate the isotherms and to concentrate them along the line of maximum shear passing through B. (Note the strong cold advection northwest of B and the weak thermal advection southeast of B.)

Horizontal *stretching deformation* tends to advect the temperature field so that the isotherms become concentrated along the axis of *dilation* (the x axis in Figure 9.1b), provided that the initial temperature field has a finite gradient along the axis of *contraction* (the y axis in Figure 9.1b). That this effect is represented by the second term on the right in (9.1) can be verified by noting from Figure 9.1b that $\partial T/\partial y < 0$ and $\partial u_g/\partial x > 0$.
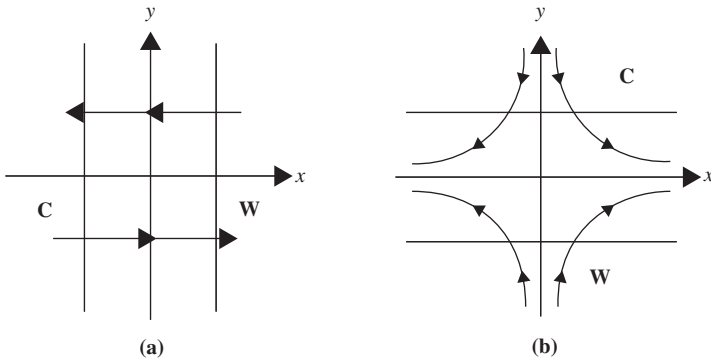
FIGURE 9.1   Frontogenetic flow configurations: (a) shows horizontal shearing deformation and (b) shows horizontal stretching deformation.
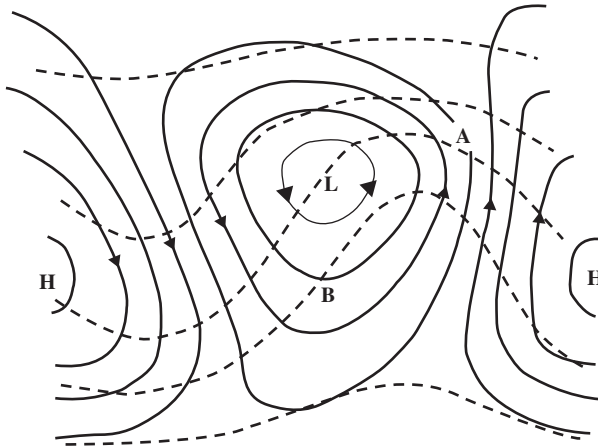
FIGURE 9.2   Schematic surface isobars (*solid lines*) and isotherms (*dashed lines*) for a baroclinic wave disturbance. *Arrows* show direction of geostrophic wind. Horizontal stretching deformation intensifies the temperature gradient at A, and horizontal shear deformation intensifies the gradient at B. (*After Hoskins and Bretherton, 1972. Copyright © American Meteorological Society. Reprinted with permission.*)

The velocity field shown in Figure 9.1b is a pure stretching deformation field. A pure deformation field is both irrotational and nondivergent. Thus, a parcel advected by a pure deformation field will merely have its shape changed in time, without any rotation or change in horizontal area. The deformation field of Figure 9.1b has a streamfunction given by $\psi = -Kxy$, where K is a constant. Such a field is characterized by the rate at which advection changes the shape of a horizontal area element. This can be illustrated by considering the rectangular element with sides δx and δy. The shape can be represented by the ratio $\delta x / \delta y$,

and the fractional rate of change of shape can thus be expressed as

$$\frac{1}{(\delta x/\delta y)}\frac{D(\delta x/\delta y)}{Dt} = \frac{1}{\delta x}\frac{D\delta x}{Dt} - \frac{1}{\delta y}\frac{D\delta y}{Dt} = \frac{\delta u}{\delta x} - \frac{\delta v}{\delta y} \approx \frac{\partial u}{\partial x} - \frac{\partial v}{\partial y}$$

It is easily verified that the fractional rate of change of $\delta x/\delta y$ for the velocity field in Figure 9.1b equals $+2K$. Thus, a square parcel with sides parallel to the x and y axes would be deformed into a rectangle as the sides parallel to the x axis stretch and those parallel to the y axis contract in time at a constant rate.

Horizontal deformation at low levels is an important mechanism for the development of both cold and warm fronts. In the example of Figure 9.2 the flow near point A has $\partial u/\partial x > 0$ and $\partial v/\partial y < 0$ so that there is a stretching deformation field present with its axis of contraction nearly orthogonal to the isotherms. This deformation field leads to strong warm advection south of point A and a weak warm advection north of point A.

Although, as shown in Figure 9.2, the low-level flow in the vicinity of a developing warm front may resemble a pure deformation field, the total flow in the upper troposphere in baroclinic disturbances seldom resembles that of a pure deformation field due to the presence of strong mean westerlies. Rather, a combination of mean flow plus horizontal stretching deformation produces a *confluent* flow as shown in Figure 9.3. Such confluence acts to concentrate the cross-stream temperature gradient as parcels move downstream. Confluent regions are always present in the tropospheric jetstream due to the influence of quasi-stationary planetary-scale waves on the position and intensity of the jet. In fact, even a monthly mean 500-hPa chart (refer to Figure 6.3) reveals two regions of large-scale confluence immediately to the east of the continents of Asia and North America. Observationally, these two regions are known to be regions of intense baroclinic wave development and frontogenesis.
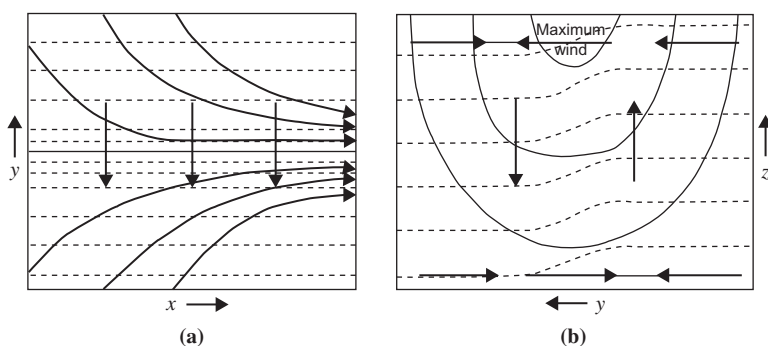
FIGURE 9.3   (a) Horizontal streamlines, isotherms, and **Q**-vectors in a frontogenetic confluence. (b) Vertical section across the confluence showing isotachs (*solid lines*), isotherms (*dashed lines*), and vertical and transverse motions (*arrows*). (*After Sawyer, 1956. Copyright © The Royal Society. Reprinted with permission.*)

The mechanisms of horizontal shear and horizontal stretching deformation discussed previously operate to concentrate the pole–equator temperature gradient on the synoptic scale ($\sim$1000 km). The time scale on which these processes operate can be estimated with the aid of (9.1). Suppose that the geostrophic wind consists of a pure deformation field so that $u_g = Kx$, and $v_g = -Ky$, and let T be a function of y only. Then (9.1) simplifies to

$$\frac{D_g}{Dt}\left(\frac{\partial T}{\partial y}\right) = K\frac{\partial T}{\partial y}$$

so that following the geostrophic motion

$$\frac{\partial T}{\partial y} = e^{Kt}\left(\frac{\partial T}{\partial y}\right)_{t=0}$$

Typically, $K \sim 10^{-5}$ s^{-1} so that the temperature gradient amplifies by a factor of 10 in about 3 days. This is much slower than observed rates of atmospheric frontogenesis.

Thus, geostrophic deformation fields alone cannot cause the rapid frontogenesis often observed in extratropical systems, in which the temperature gradient can become concentrated in a zone of $\sim$50 km width on a time scale of less than a day. This rapid reduction in scale is caused primarily by the frontogenetic character of the secondary circulation driven by the quasi-geostrophic synoptic-scale flow (moist processes may also be important in rapid frontogenesis).

The nature of the secondary flow may be deduced from the pattern of **Q** vectors illustrated in Figure 9.3a. As discussed in Section 6.5, the divergence of **Q** forces a secondary ageostrophic circulation. For the situation of Figure 9.3, this circulation is in the cross-frontal plane as illustrated in Figure 9.3b. Advection of the temperature field by this ageostrophic circulation tends to increase the horizontal temperature gradient at the surface on the warm side of the jet axis. Temperature advection by the upper-level secondary circulation, however, tends to concentrate the temperature gradient on the cold side of the jet axis. As a result, the frontal zone tends to slope toward the cold air side with height. The differential vertical motion associated with the ageostrophic circulation tends to weaken the front in the midtroposphere due to adiabatic temperature changes (adiabatic warming on the cold side of the front and adiabatic cooling on the warm side). For this reason fronts are most intense in the lower troposphere and near the tropopause.

The secondary circulation associated with frontogenesis is required to maintain the thermal wind balance between the along-front flow and the cross-front temperature gradient in the presence of advective processes that tend to destroy this balance. The concentration of the isotherms by the horizontal advection increases the cross-stream pressure gradient at upper levels, and thus requires an increase in the vertical shear of the along-jet flow in order to maintain thermal wind balance. The required upper-level acceleration of the jet is produced by the Coriolis force caused by the cross-jet ageostrophic wind, which develops

in response to the increased cross-stream pressure gradient in the jetstream core. As the jet accelerates, cyclonic vorticity must be generated on the cold side of the jet axis and anticyclonic vorticity on the warm side. These vorticity changes require that the horizontal flow at the jetstream level be convergent on the cold side of the jet axis and divergent on the warm side of the jet axis. The resulting vertical circulation and low-level secondary ageostrophic motion required by mass continuity are indicated in Figure 9.3b.

9.2.2 Semigeostrophic Theory

To analyze the dynamics of the frontogenetic motion fields discussed in the previous subsection, it is convenient to use the Boussinesq approximation introduced in Section 2.8, in which density is replaced by a constant reference value ρ_0 except where it appears in the buoyancy force. This approximation simplifies the equations of motion without affecting the main features of the results. It is also useful to replace the total pressure and density fields with deviations from their standard atmosphere values. Thus, we let $\Phi(x, y, z, t) = (p - p_0)/\rho_0$ designate the pressure deviation normalized by density and $\Theta = \theta - \theta_0$ designate the potential temperature deviation, where $p_0(z)$ and $\theta_0(z)$ are the height-dependent standard atmosphere values of pressure and potential temperature, respectively.

With the preceding definitions, the horizontal momentum equations, thermodynamic energy equation, hydrostatic approximation, and continuity equation become

$$\frac{Du}{Dt} - fv + \frac{\partial \Phi}{\partial x} = 0 \tag{9.2}$$

$$\frac{Dv}{Dt} + fu + \frac{\partial \Phi}{\partial y} = 0 \tag{9.3}$$

$$\frac{D\Theta}{Dt} + w\frac{d\theta_0}{dz} = 0 \tag{9.4}$$

$$b \equiv \frac{g\Theta}{\theta_{00}} = \frac{\partial \Phi}{\partial z} \tag{9.5}$$

$$\frac{\partial u}{\partial x} + \frac{\partial v}{\partial y} + \frac{\partial w}{\partial z} = 0 \tag{9.6}$$

where b is the *buoyancy*, θ_{00} is a constant reference value of potential temperature, and

$$\frac{D}{Dt} \equiv \frac{\partial}{\partial t} + u\frac{\partial}{\partial x} + v\frac{\partial}{\partial y} + w\frac{\partial}{\partial z}$$

From the discussion of the previous subsection it should be clear that the horizontal scale of variations parallel to a front is much larger than the cross-frontal scale. This scale separation suggests that to a first approximation we can model fronts as two-dimensional structures. For convenience we choose
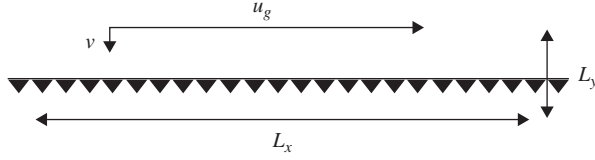
FIGURE 9.4   Velocity and length scales relative to a front parallel to the *x* axis.

a coordinate system in which the front is stationary and take the cross-frontal direction to be parallel to the *y* axis. Then $L_x \gg L_y$, where L_x and L_y designate the along-front and cross-front length scales. Similarly, $U \gg V$, where U and V, respectively, designate the along-front and cross-front velocity scales. Figure 9.4 shows these scales relative to the front.

Letting $U \sim 10 \text{ m s}^{-1}$, $V \sim 1 \text{ m s}^{-1}$, $L_x \sim 1000$ km, and $L_y \sim 100$ km, we find that it is possible to use the differing scales of the along-front and cross-front motion to simplify the dynamics. Assuming that $D/Dt \sim V/L_y$ (the cross-front advection time scale) and defining a Rossby number, $\text{Ro} \equiv V/fL_y \ll 1$, the magnitude of the ratios of the inertial and Coriolis terms in the *x* and *y* components of the momentum equation can be expressed as

$$\frac{|Du/Dt|}{|fv|} \sim \frac{UV/L_y}{fV} \sim \text{Ro}\left(\frac{U}{V}\right) \sim 1$$

$$\frac{|Dv/Dt|}{|fu|} \sim \frac{V^2/L_y}{fU} \sim \text{Ro}\left(\frac{V}{U}\right) \sim 10^{-2}$$

The along-front velocity is in geostrophic balance with the cross-front pressure gradient with error of order 1%, but geostrophy does not hold even approximately for the cross-front velocity. Therefore, if the geostrophic wind components are defined by

$$fu_g = -\partial\Phi/\partial y, \qquad fv_g = \partial\Phi/\partial x$$

and we separate the horizontal velocity field into geostrophic and ageostrophic parts, to a good approximation $u = u_g$, but $v = v_g + v_a$, where v_g and v_a are the same order of magnitude.

The *x* component of the horizontal momentum equation (9.2), the thermodynamic energy equation (9.4), and the continuity equation (9.6) for frontal scaling can thus be expressed as

$$\frac{Du_g}{Dt} - fv_a = 0 \tag{9.7}$$

$$\frac{Db}{Dt} + wN^2 = 0 \tag{9.8}$$

$$\frac{\partial v_a}{\partial y} + \frac{\partial w}{\partial z} = 0 \tag{9.9}$$

Here, (9.8) is obtained by using (9.5) to replace Θ by b in (9.4), and N is the buoyancy frequency defined in terms of potential temperature as

$$N^2 \equiv \frac{g}{\theta_{00}} \frac{\partial \theta_0}{\partial z}$$

Because the along-front velocity is in geostrophic balance, u_g and b are related by the thermal wind relationship:

$$f \frac{\partial u_g}{\partial z} = -\frac{\partial b}{\partial y} \tag{9.10}$$

Note that (9.7) and (9.8) differ from their quasi-geostrophic analogs; although zonal momentum is still approximated geostrophically, and advection parallel to the front is geostrophic, the advection of momentum and temperature across the front is due not only to the geostrophic wind but to the ageostrophic (v_a, w) circulation:

$$\frac{D}{Dt} = \frac{D_g}{Dt} + \left(v_a \frac{\partial}{\partial y} + w \frac{\partial}{\partial z} \right)$$

where D_g/Dt was defined in equation (6.5). Replacement of momentum by its geostrophic value in (9.7) is referred to as the *geostrophic momentum* approximation, and the set of prediction equations that result are called the *semigeostrophic* equations.[1]

9.2.3 Cross-Frontal Circulation

Equations (9.7) through (9.10) form a closed set that can be used to determine the cross-frontal ageostrophic circulation in terms of the distribution of zonal wind or temperature. Suppose that the large-scale geostrophic flow is acting to intensify the north–south temperature gradient through deformation as shown in Figure 9.3. As the temperature gradient increases, the vertical shear of the zonal wind must also increase to maintain geostrophic balance. This requires an increase of u_g in the upper troposphere, which must be produced by the Coriolis force associated with a cross-frontal ageostrophic circulation—see (9.7). The structure of this secondary circulation can be computed by deriving an equation analogous to the omega equation discussed in Section 6.5.

We first differentiate (9.8) with respect to y and use the chain rule to express the result as

$$\frac{D}{Dt} \left(\frac{\partial b}{\partial y} \right) = Q_2 - \frac{\partial v_a}{\partial y} \frac{\partial b}{\partial y} - \frac{\partial w}{\partial y} \left(N^2 + \frac{\partial b}{\partial z} \right) \tag{9.11}$$

---

[1] Some authors reserve this name for a version of the equations written in a transformed set of coordinates called geostrophic coordinates (e.g., Hoskins, 1975).

where

$$Q_2 = -\frac{\partial u_g}{\partial y}\frac{\partial b}{\partial x} - \frac{\partial v_g}{\partial y}\frac{\partial b}{\partial y} \tag{9.12}$$

is just the y component of the **Q** vector discussed in Section 6.5, but expressed in the Boussinesq approximation.

Next we differentiate equation (9.7) with respect to z, again use the chain rule to rearrange terms, and use the thermal wind equation (9.10) to replace $\partial u_g/\partial z$ by $\partial b/\partial y$ on the right side. The result can then be written as

$$\frac{D}{Dt}\left(f\frac{\partial u_g}{\partial z}\right) = Q_2 + \frac{\partial v_a}{\partial z}f\left(f - \frac{\partial u_g}{\partial y}\right) + \frac{\partial w}{\partial z}\frac{\partial b}{\partial y} \tag{9.13}$$

Again, as shown in Section 6.5, the geostrophic forcing (given by Q_2) tends to destroy thermal wind balance by changing the temperature gradient and vertical shear parts of the thermal wind equation in equal but opposite senses. This tendency of geostrophic advection to destroy geostrophic balance is counteracted by the cross-frontal secondary circulation.

In this case the secondary circulation is a two-dimensional transverse circulation in the y, z plane. It can thus be represented in terms of a meridional streamfunction ψ_M defined so that

$$v_a = -\partial\psi_M/\partial z, \qquad w = \partial\psi_M/\partial y \tag{9.14}$$

which identically satisfies the continuity equation (9.9). Adding (9.11) and (9.13), and using the thermal wind balance (9.10) to eliminate the time derivative and (9.14) to eliminate v_a and w, we obtain the *Sawyer–Eliassen equation*:

$$N_s^2\frac{\partial^2\psi_M}{\partial y^2} + F^2\frac{\partial^2\psi_M}{\partial z^2} + 2S^2\frac{\partial^2\psi_M}{\partial y\partial z} = 2Q_2 \tag{9.15}$$

where

$$N_s^2 \equiv N^2 + \frac{\partial b}{\partial z}, \quad F^2 \equiv f\left(f - \frac{\partial u_g}{\partial y}\right) = f\frac{\partial M}{\partial y}, \quad S^2 \equiv -\frac{\partial b}{\partial y} \tag{9.16}$$

where M is the absolute momentum defined as

$$M = fy - u_g$$

Equation (9.15) can be compared with the quasi-geostrophic version obtained by neglecting advection by the ageostrophic circulation in (9.7) and (9.8). This has the form

$$N^2\frac{\partial^2\psi_M}{\partial y^2} + f^2\frac{\partial^2\psi_M}{\partial z^2} = 2Q_2 \tag{9.17}$$

Thus, in the quasi-geostrophic case the coefficients in the differential operator on the left depend only on the standard atmosphere static stability, N, and the planetary vorticity, f, whereas in the semigeostrophic case they depend on the deviation of potential temperature from its standard profile through the N_s and S terms and the absolute vorticity through the F term.

An equation of the form (9.17), in which the coefficients of the derivatives on the left are positive, is referred to as an *elliptic boundary value problem*. It has a solution ψ_M that is uniquely determined by Q_2 plus the boundary conditions. For a situation such as that of Figure 9.1b, with both $\partial v_g / \partial y$ and $\partial b / \partial y$ negative, the forcing term Q_2 is negative in the frontal region. The streamfunction in that case describes a circulation symmetric about the y axis, with rising on the warm side and sinking on the cold side. The semigeostrophic case (9.15) is also an elliptic boundary value problem provided that $N_s^2 F^2 - S^4 > 0$. It can be shown (see Problem 9.1) that this condition requires that the Ertel potential vorticity be positive in the Northern Hemisphere and negative in the Southern Hemisphere, which is nearly always the case in the extratropics for an unsaturated atmosphere.

The spatial variation of the coefficients in (9.16) and the presence of the cross-derivative term produce a distortion of the secondary circulation, as shown in Figure 9.5. The frontal zone slopes toward the cold air side with height; there is an intensification of the cross-frontal flow near the surface in the region of large absolute vorticity on the warm air side of the front and a tilting of the circulation with height.

The influence of the ageostrophic circulation on the time scale for frontogenesis can be illustrated by comparing the processes included in quasi-geostrophic and semigeostrophic frontogenesis. For semigeostrophic advection there is a positive feedback that greatly reduces the time scale of frontogenesis compared
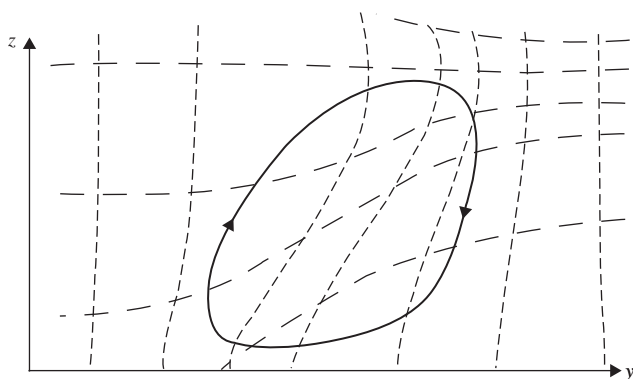
FIGURE 9.5 Relationship of the ageostrophic circulation (*heavy curve with arrows*) in two-dimensional frontogenesis to the potential temperature field (*long dashes*) and absolute momentum field (*short dashes*). Cold air is on the right and warm air is on the left. Note the tilt of the circulation toward the cold air side and the enhanced gradients of the absolute momentum and potential temperature fields in the frontal zone.

to that in the quasi-geostrophic case. As the temperature contrast increases, Q_2 increases, and the secondary circulation must also increase so that the amplification *rate* of $|\partial T/\partial y|$ increases with $|\partial T/\partial y|$ rather than remaining constant as in the quasi-geostrophic case. Because of this feedback, in the absence of frictional effects, the semigeostrophic model can produce an infinite temperature gradient at the surface in less than half a day.

9.3   SYMMETRIC BAROCLINIC INSTABILITY

Observations indicate that mesoscale bands of cloud and precipitation commonly occur in association with synoptic-scale systems. These are often aligned with fronts but are separate entities. In common with fronts, such features are generally associated with strong baroclinicity and have length scales parallel to the mean wind shear that much larger than the scales across the wind shear. A plausible source for such features is a two-dimensional form of baroclinic instability known as *symmetric instability* (also referred to as slantwise convection).

For typical atmospheric conditions, buoyancy tends to stabilize air parcels against vertical displacements, and rotation tends to stabilize parcels with respect to horizontal displacements. Instability with respect to vertical displacements is referred to as hydrostatic (or, simply, static) instability (see Section 2.7.3). For an unsaturated atmosphere, static stability requires that the local buoyancy frequency squared be positive ($N_s^2 > 0$). Instability with respect to horizontal displacements, however, is referred to as inertial instability (see Section 5.5.1). The condition for inertial stability equation (5.74) requires that F^2 as defined in (9.16) be positive.

If parcels are displaced along slantwise paths rather than vertical or horizontal paths, it is possible under certain conditions for the displacements to be unstable even when the conditions for ordinary static and inertial stability are separately satisfied. Such instability can occur only in the presence of vertical shear of the mean horizontal wind and may be regarded as a special form of baroclinic instability in which the perturbations are independent of the coordinate parallel to the mean flow. Alternatively, as will be shown, symmetric instability may be regarded as isentropic inertial instability.

For convenience in deriving the conditions for symmetric instability, we use the Boussinesq equations of Section 2.8 and assume that the flow is independent of the x coordinate. The mean wind is directed along the x axis and is in thermal wind balance with the meridional temperature gradient:

$$f\partial u_g/\partial z = -\partial b/\partial y = -(g/\theta_{00})\,\partial\Theta/\partial y \qquad (9.18)$$

where, as before, θ_{00} is a constant reference value of potential temperature.

Following Sections 2.7.3 and 5.5.1, we measure the stability with respect to vertical displacements by the distribution of total potential temperature $\theta = \theta_0 + \Theta$ and that with respect to horizontal displacements by the distribution of

the absolute zonal momentum, $M \equiv fy - u_g$ (where $\partial M/\partial y = f - \partial u_g/\partial y$ is the zonal mean absolute vorticity).

For a barotropic flow, potential temperature surfaces are oriented horizontally and absolute momentum surfaces are oriented vertically in the meridional plane. When the mean flow is westerly and increases with height, however, the potential temperature and absolute momentum surfaces both slope upward toward the pole. The comparative strengths of the vertical and horizontal restoring forces in the midlatitude troposphere are given by the ratio $N_s^2/(f\partial M/\partial y)$. For typical tropospheric conditions, this ratio is $\sim 10^4$. Thus, parcel motion in the plane orthogonal to the mean flow will remain much closer to θ surfaces than to M surfaces. It is thus natural to utilize isentropic coordinates to analyze parcel displacements. The arguments of Section 5.5.1 still apply, provided that derivatives with respect to y are taken at constant θ. The stability of such motions thus depends on the relative slope of the θ and M surfaces. Ordinarily the M surfaces will slope more than the θ surfaces (see Figure 9.5), and parcel displacements are stable. However, when the θ surfaces slope more than the M surfaces so that

$$f(\partial M/\partial y)_\theta < 0 \qquad (9.19)$$

the flow is unstable with respect to displacements along the θ surfaces. This situation may occur in regions of a very strong horizontal temperature gradient and weak vertical stability. The condition in (9.19) is similar to the criterion of (5.74) for inertial instability, except that the derivative of M is here taken along a sloping θ surface.

If (9.19) is multiplied by $-g(\partial\theta/\partial p)$, the criterion for symmetric instability can be expressed in terms of the distribution of Ertel potential vorticity (4.12) in the simple form

$$f\bar{P} < 0 \qquad (9.20)$$

where $\bar{P}$ is the potential vorticity of the basic state geostrophic flow. Thus, if the initial state potential vorticity in the Northern Hemisphere is everywhere positive, then symmetric instability cannot develop through adiabatic motions, as potential vorticity is conserved following the motion and will always remain positive.

To demonstrate that (9.19) is the condition for symmetric instability, we consider the change in mean kinetic energy required for exchange of the tubes of fluid labeled 1 and 2 in Figure 9.6. (These tubes are located at y_1 and $y_2 = y_1 + \delta y$, respectively, and are assumed to extend infinitely along the x axis so that the problem is two-dimensional.) Because the tubes lie on the same potential temperature surface, they have the same available potential energy. Thus, a spontaneous exchange of parcels is possible if $\delta(\text{KE})$, the kinetic energy of the zonal flow after exchange minus that in the initial state, is negative. Otherwise some external source of energy is required to furnish the kinetic energy of the meridional and vertical motions required for the exchange.
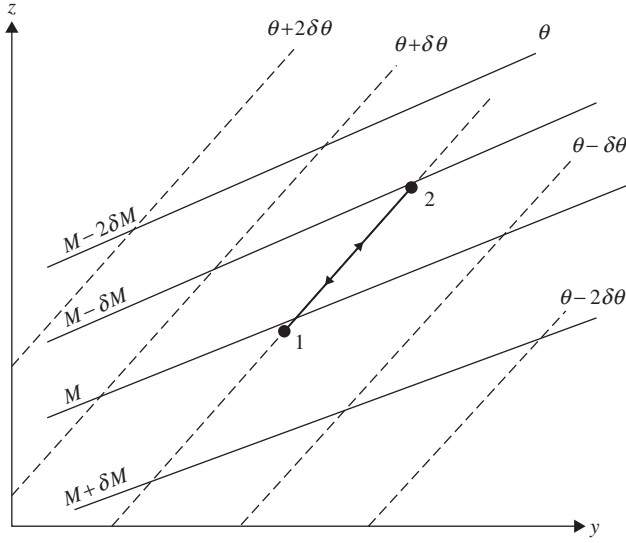
FIGURE 9.6 Cross-section showing isolines of absolute momentum and potential temperature for a symmetrically unstable basic state. Motion along the isentropic path between points labeled 1 and 2 is unstable, as M decreases with latitude along the path. See text for details.

Initially the motion of the tubes is parallel to the x axis and in geostrophic balance so that the absolute momentum for the two tubes is

$$
\begin{aligned}
M_1 &= fy_1 - u_1 = fy_1 - u_g(y_1, z) \\
M_2 &= fy_2 - u_2 = fy_1 + f\delta y - u_g(y_1 + \delta y, z + \delta z)
\end{aligned}
\tag{9.21}
$$

Absolute momentum is conserved by the tubes so that after exchange the perturbation zonal velocities are given by

$$
M_1' = fy_1 + f\delta y - u_1' = M_1, \quad M_2' = fy_1 - u_2' = M_2
\tag{9.22}
$$

Eliminating M_1 and M_2 between (9.21) and (9.22) and solving for the disturbance zonal wind, we obtain

$$
u_1' = f\delta y + u_1, \quad u_2' = -f\delta y + u_2
$$

The difference in zonal kinetic energy between the final state and the initial state is given by

$$
\begin{aligned}
\delta(\text{KE}) &= \tfrac{1}{2}\left(u_1'^2 + u_2'^2\right) - \tfrac{1}{2}\left(u_1^2 + u_2^2\right) \\
&= f\delta y\,(u_1 - u_2 + f\delta y) = f\delta y\,(M_2 - M_1)
\end{aligned}
\tag{9.23}
$$

Thus, $\delta(\text{KE})$ is negative, and unforced meridional motion may occur, provided that $f(M_2 - M_1) < 0$. This is equivalent to the condition (9.19), as the tubes lie along the same θ surface.

To estimate the likelihood that conditions for symmetric instability may be satisfied, it is useful to express the stability criterion in terms of a mean-flow *Richardson number*. To do this we first note that the slope of an M surface can be estimated from noting that on an M surface

$$\delta M = \frac{\partial M}{\partial y}\delta y + \frac{\partial M}{\partial z}\delta z = 0$$

so that the ratio of δz to δy at constant M is

$$\left(\frac{\delta z}{\delta y}\right)_M = \left(-\frac{\partial M}{\partial y}\right) \bigg/ \left(\frac{\partial M}{\partial z}\right) = \left(f - \frac{\partial u_g}{\partial y}\right) \bigg/ \left(\frac{\partial u_g}{\partial z}\right) \tag{9.24}$$

Similarly, the slope of a potential temperature surface is

$$\left(\frac{\delta z}{\delta y}\right)_\theta = \left(-\frac{\partial \theta}{\partial y}\right) \bigg/ \left(\frac{\partial \theta}{\partial z}\right) = \left(f\frac{\partial u_g}{\partial z}\right) \bigg/ \left(\frac{g}{\theta_{00}} \frac{\partial \theta}{\partial z}\right) \tag{9.25}$$

where we have used the thermal wind relationship to express the meridional temperature gradient in terms of the vertical shear of the zonal wind. The ratio of (9.24) to (9.25) is simply

$$\left(\frac{\delta z}{\delta y}\right)_M \bigg/ \left(\frac{\delta z}{\delta y}\right)_\theta = f\left(f - \frac{\partial u_g}{\partial y}\right)\left(\frac{g}{\theta_{00}}\frac{\partial \theta}{\partial z}\right) \bigg/ \left[f^2 \left(\frac{\partial u_g}{\partial z}\right)^2\right] = \frac{F^2 N_s^2}{S^4}$$

where the notation in the last term is defined in (9.16).

Recalling that symmetric instability requires that the slopes of the θ surfaces exceed those of the M surfaces, the necessary condition for instability of geostrophic flow parallel to the x axis becomes

$$\left(\frac{\delta z}{\delta y}\right)_M \bigg/ \left(\frac{\delta z}{\delta y}\right)_\theta = f\left(f - \frac{\partial u_g}{\partial y}\right) \text{Ri} \big/ f^2 = \frac{F^2 N_s^2}{S^4} < 1 \tag{9.26}$$

where the mean-flow *Richardson number* Ri is defined as

$$\text{Ri} \equiv \left(\frac{g}{\theta_{00}}\frac{\partial \theta}{\partial z}\right) \bigg/ \left(\frac{\partial u_g}{\partial z}\right)^2$$

Thus, if the relative vorticity of the mean flow vanishes ($\partial u_g/\partial y = 0$), Ri < 1 is required for instability.

The condition (9.26) can be related to (9.20) by observing that (9.26) requires that $F^2 N_s^2 - S^4 < 0$ for symmetric instability. As is to be shown in Problem 9.1,

$$F^2 N_s^2 - S^4 = \left(\rho f g / \theta_{00}\right)\overline{P} \tag{9.27}$$

Because the large-scale potential vorticity, $\bar{P}$, is normally positive in the Northern Hemisphere and negative in the Southern Hemisphere, (9.27) is ordinarily positive in both hemispheres; thus, the condition for symmetric instability is rarely satisfied. If the atmosphere is saturated, however, the relevant static stability condition involves the lapse rate of the equivalent potential temperature, and neutral conditions with respect to symmetric instability may easily occur (see Section 9.5).

Finally, it is worth noting that the condition for stability with respect to symmetric displacements, $F^2 N_s^2 - S^4 > 0$, is identical to the condition that the Sawyer–Eliassen equation (9.15) be an elliptic boundary value problem. Thus, when the flow is stable with respect to symmetric baroclinic perturbations, a nonzero *forced* transverse circulation governed by (9.15) will exist when there is nonzero forcing, Q_2—see (9.12). *Free* transverse oscillations, however, may occur in the absence of forcing. These require including the horizontal acceleration term in the y component of the momentum equation. The resulting equation for the transverse circulation has the form (see Appendix F):

$$\frac{\partial^2}{\partial t^2}\left(\frac{\partial^2 \psi_M}{\partial z^2}\right) + N_s^2 \frac{\partial^2 \psi_M}{\partial y^2} + F^2 \frac{\partial^2 \psi_M}{\partial z^2} + 2S^2 \frac{\partial^2 \psi_M}{\partial y \partial z} = 0 \qquad (9.28)$$

which should be compared with (9.15). When $F^2 N_s^2 - S^4 > 0$, solutions of (9.28) correspond to stable oscillations, while for $F^2 N_s^2 - S^4 < 0$, solutions are exponentially growing, corresponding to symmetric baroclinic instability.

9.4   MOUNTAIN WAVES

When stably stratified air is forced to flow over varying surface topography, buoyancy oscillations are created. First, consider the case with constant wind and stratification for sinusoidally varying topography, and then allow for localized mountain barriers and vertical variations in static stability and wind.

9.4.1   Waves over Sinusoidal Topography

When air with mean wind speed $\bar{u}$ is forced to flow over a sinusoidal pattern of ridges under statically stable conditions, individual air parcels are alternately displaced upward and downward from their equilibrium levels and will thus undergo buoyancy oscillations as they move across the ridges, as shown in Figure 9.7. In this case there are solutions in the form of waves that are stationary relative to the ground. For such stationary waves, w' depends only on (x, z) and the equation governing their motion, (5.64), simplifies to

$$\left(\frac{\partial^2 w'}{\partial x^2} + \frac{\partial^2 w'}{\partial z^2}\right) + \frac{N^2}{\bar{u}^2} w' = 0 \qquad (9.29)$$

(a)

(b)
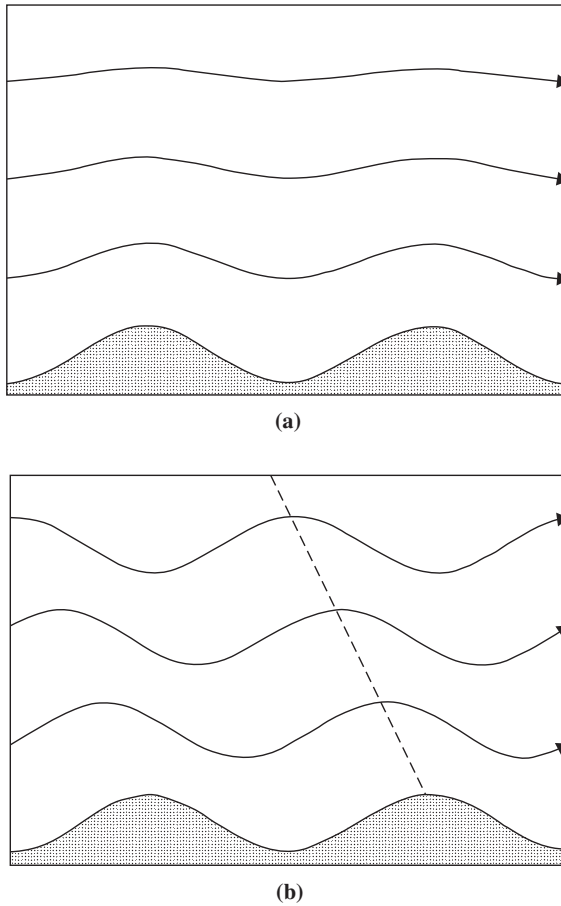
FIGURE 9.7 Streamlines in steady flow over an infinite series of sinusoidal ridges for the narrow ridge case (a) and broad ridge case (b). The *dashed line* in (b) shows the phase of maximum upward displacement. (*From Durran, 1990. Copyright © American Meteorological Society. Reprinted with permission.*)

Substituting

$$w' = \operatorname{Re} \hat{w} \exp^{i(kx+mz)} \qquad (9.30)$$

into (9.29) yields

$$m^2 = \frac{N^2}{\bar{u}^2} - k^2 \qquad (9.31)$$

For given values of N, k, and $\bar{u}$, (9.31) determines the vertical structure. Then if $|\bar{u}| < N/k$, (9.31) shows that $m^2 > 0$ (i.e., m must be real) and solutions of (9.29) have the form of vertically propagating waves. When $m^2 < 0$, $m = im_i$

is imaginary and the solution to (9.29) will have the form of vertically trapped waves:

$$w' = \hat{w} \exp(ikx) \exp(-m_i z)$$

Thus, vertical propagation is possible only when $|\bar{u}k|$, the magnitude of the frequency relative to the mean flow, is less than the buoyancy frequency.

Stable stratification, wide ridges, and comparatively weak zonal flow provide favorable conditions for the formation of vertically propagating topographic waves (m real). Because the energy source for these waves is at the ground, they must transport energy upward. Hence, the phase speed relative to the mean zonal flow must have a downward component. Thus, if $\bar{u} > 0$, lines of constant phase must tilt westward with height. When m is imaginary, however, the solution (9.30) has exponential behavior in the vertical with an exponential decay height of μ^{-1}, where $\mu = |m|$. Boundedness as $z \to \infty$ requires that we choose the solution with exponential decay away from the lower boundary.

To contrast the character of the solutions for real and imaginary m, we consider a specific example in which there is westerly mean flow over topography with a height profile given by

$$h(x) = h_M \cos kx$$

where h_M is the amplitude of the topography. Then, because the flow at the lower boundary must be parallel to the boundary, the vertical velocity perturbation at the boundary is given by the rate at which the boundary height changes following the motion:

$$w'(x, 0) = \left(Dh/Dt\right)_{z=0} \approx \bar{u}\partial h/\partial x = -\bar{u}kh_M \sin kx$$

and the solution of (9.29) that satisfies this condition can be written

$$w(x, z) = \left\{ \begin{array}{ll} -\bar{u}h_M k e^{-\mu z} \sin kx, & \bar{u}k > N \\ -\bar{u}h_M k \sin(kx + mz), & \bar{u}k < N \end{array} \right\} \tag{9.32}$$

For fixed mean wind and buoyancy frequency, the character of the solution depends only on the horizontal scale of the topography. The two cases of (9.32) may be regarded as narrow ridge and wide ridge cases, respectively, since for specified values of $\bar{u}$ and N, the character of the solution is determined by the zonal wave number k. The streamline patterns corresponding to these cases for westerly flow are illustrated in Figure 9.7. In the narrow ridge case (Figure 9.7a), the maximum upward displacement occurs at the ridge tops, and the amplitude of the disturbance decays with height. In the wide ridge case (Figure 9.7b), the line of maximum upward displacement tilts back toward the west ($m > 0$), and amplitude is independent of height consistent with an internal gravity wave propagating westward relative to the mean flow.

Alternatively, for fixed zonal wave number and buoyancy frequency, the solution depends only on the speed of the mean zonal wind. As indicated in

(9.32), only for mean zonal wind magnitudes less than the critical value N/k will vertical wave propagation occur.

Equation (9.29) was obtained for conditions of constant basic state flow. In reality, both the zonal wind $\bar{u}$ and the stability parameter N generally vary with height, and ridges are usually isolated rather than periodic. A wide variety of responses are possible depending on the shape of the terrain and on wind and stability profiles. Under certain conditions, large-amplitude waves can be formed, which may generate severe downslope surface winds and zones of strong clear air turbulence. Such circulations are discussed further in Section 9.4.4.

9.4.2 Flow over Isolated Ridges

Just as flow over a periodic series of sinusoidal ridges can be represented by a single sinusoidal function flow—that is, by a single Fourier harmonic flow—over an isolated ridge can be approximated by the sum of a number of Fourier components (see Section 5.2.1). Thus, any zonally varying topography can be represented by a Fourier series of the form

$$h_M(x) = \sum_{s=1}^{\infty} \mathrm{Re}\left[h_s \exp(ik_s x)\right] \tag{9.33}$$

where h_s is the amplitude of the sth Fourier component of the topography. We can then express the solution to the wave equation (9.29) as the sum of Fourier components:

$$w(x,z) = \sum_{s=1}^{\infty} \mathrm{Re}\left\{W_s \exp\left[i\left(k_s x + m_s z\right)\right]\right\} \tag{9.34}$$

where $W_s = ik_s \bar{u} h_s$, and $m_s^2 = N^2/\bar{u}^2 - k_s^2$.

Individual Fourier modes will yield vertically propagating or vertically decaying contributions to the total solution (9.34) depending on whether m_s is real or imaginary. This in turn depends on whether k_s^2 is less than or greater than $N^2/\bar{u}^2$. Thus, each Fourier mode behaves just as the solution (9.30) for periodic sinusoidal topography behaves. For a narrow ridge, Fourier components with wave numbers greater than $N/\bar{u}$ dominate in (9.33), and the resulting disturbance decays with height. For a broad ridge, components with wave numbers less than $N/\bar{u}$ dominate, and the disturbance propagates vertically. In the wide mountain limit where $m_s^2 \approx N^2/\bar{u}^2$, the flow is periodic in the vertical with a vertical wavelength of $2\pi m_s^{-1}$, and phase lines tilt upstream with height as shown in Figure 9.8.

Vertically propagating gravity waves generated by flow over broad topography can produce clouds both upstream and downstream of the topography depending on variations of the moisture distribution with altitude. In the example shown in Figure 9.7, the positions labeled A and B indicate regions where
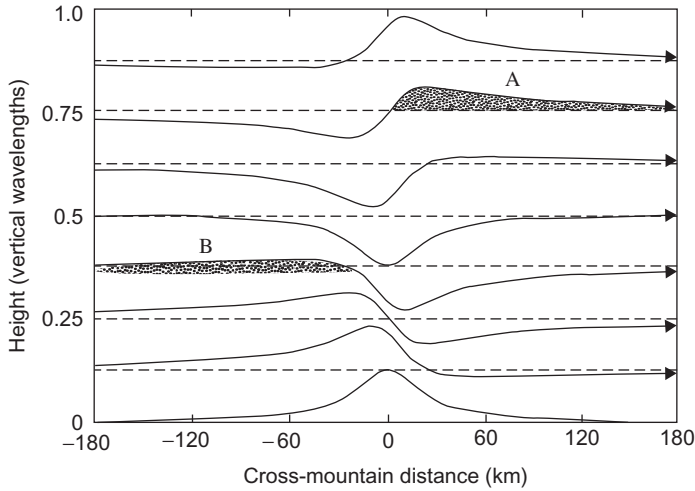
FIGURE 9.8 Streamlines of flow over a broad isolated ridge showing upstream phase tilt with height. The pattern is periodic in height, and one vertical wavelength is shown. Orographic clouds may form in the shaded areas where streamlines are displaced upward from equilibrium either upstream or downstream of the ridge if sufficient moisture is present. (*After Durran, 1990. Copyright © American Meteorological Society. Reprinted with permission.*)

streamlines are displaced upward downstream and upstream of the ridge, respectively. If sufficient moisture is present, orographic clouds may then form in region A or B as suggested by the shading in Figure 9.8.

9.4.3 Lee Waves

If $\bar{u}$ and N are allowed to vary in height, then (9.29) must be replaced by

$$\left(\frac{\partial^2 w'}{\partial x^2} + \frac{\partial^2 w'}{\partial z^2}\right) + l^2 w' = 0 \qquad (9.35)$$

where the *Scorer parameter*, l, is defined as

$$l^2 = N^2 \left/ \bar{u}^2 - \bar{u}^{-1} d^2 \bar{u} \right/ dz^2$$

and the condition for vertical propagation becomes $k_s^2 < l^2$.

   If the mean cross-mountain wind speed increases strongly with height, or if there is a low-level stable layer so that N decreases strongly with height, there may be a layer near the surface in which vertically propagating waves are permitted, which is topped by a layer in which the disturbance decays in the vertical. In that case vertically propagating waves in the lower layer are reflected when they reach the upper layer. Under some circumstances the waves may be repeatedly reflected from the upper layer and the surface downstream of the mountain, leading to a series of "trapped" lee waves as shown in Figure 9.9.
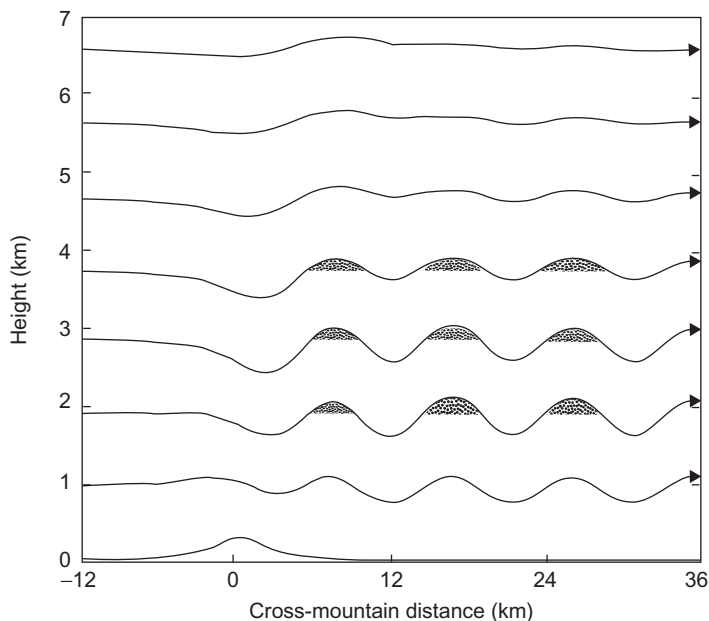
FIGURE 9.9   Streamlines for trapped lee waves generated by flow over topography with vertical variation of the Scorer parameter. *Shading* shows locations where lee wave clouds may form. (*After Durran, 1990. Copyright © American Meteorological Society. Reprinted with permission.*)

Vertical variations in the Scorer parameter can also modify the amplitude of waves that are sufficiently long to propagate vertically through the entire troposphere. Amplitude enhancement leading to wave breaking and turbulent mixing can occur if there is a *critical level* where the mean flow goes to zero ($l \rightarrow \infty$).

9.4.4   Downslope Windstorms

Strong downslope surface winds are occasionally observed along the lee slopes of mountain ranges. Although partial reflection of vertically propagating linear gravity waves may produce enhanced surface winds under some conditions, it appears that nonlinear processes are essential to account for observed windstorms associated with stable flow over topography.

To demonstrate the role of nonlinearity, we assume that the troposphere has a stable lower layer of undisturbed depth h topped by a weakly stable upper layer, and assume that the lower layer behaves as a barotropic fluid with a free surface $h(x,t)$. We assume that disturbances have zonal wavelengths much greater than the layer depth. The motion of the lower layer may then be described by the shallow water equations of Section 4.5, but with the lower boundary

condition replaced by

$$w(x, h_M) = Dh_M / Dt = u \partial h_M / \partial x$$

where h_M again denotes the height of the topography.

We first examine the linear behavior of this model by considering steady flow over small-amplitude topography. Neglecting ambient rotation, the linearized shallow water equations in steady state become

$$\bar{u} \frac{\partial u'}{\partial x} + g \frac{\partial h'}{\partial x} = 0 \qquad (9.36)$$

$$\bar{u} \frac{\partial (h' - h_M)}{\partial x} + H \frac{\partial u'}{\partial x} = 0 \qquad (9.37)$$

Here, $h' = h - H$, where H is the mean height of the interface and $h' - h_M$ is the deviation from H of the thickness of the layer.

The solutions for (9.36) and (9.37) can be expressed as

$$h' = -\frac{h_M \left(\bar{u}^2 / c^2\right)}{\left(1 - \bar{u}^2 / c^2\right)}, \quad u' = \frac{h_M}{H} \left(\frac{\bar{u}}{1 - \bar{u}^2 / c^2}\right) \qquad (9.38)$$

where $c^2 \equiv gH$ is the shallow water gravity wave speed. The characteristics of the disturbance fields h' and u' depend on the magnitude of the mean-flow *Froude number*, defined by the relation $\mathrm{Fr}^2 = \bar{u}^2 / c^2$. When Fr < 1, the flow is referred to as *subcritical*. In subcritical flow, the shallow water gravity wave speed is greater than the mean-flow speed, and the disturbance height and wind fields are out of phase. The interface height disturbance is negative, and the velocity disturbance is positive over the topographic barrier as shown in Figure 9.10a. When Fr > 1, the flow is referred to as *supercritical*. In supercritical flow the mean flow exceeds the shallow water gravity wave speed. Gravity waves cannot play a role in establishing the steady-state adjustment between height and velocity disturbances because such waves are swept downstream from the ridge by the mean flow. In this case the fluid thickens and slows as it ascends over the barrier (Figure 9.10b). It is also clear from (9.38) that for Fr ∼1 the perturbations are no longer small and the linear solution breaks down.

The nonlinear equations corresponding to (9.36) and (9.37) can be expressed as

$$u \frac{\partial u}{\partial x} + g \frac{\partial h}{\partial x} = 0 \qquad (9.39)$$

$$\frac{\partial}{\partial x} \left[u(h - h_M) \right] = 0 \qquad (9.40)$$

Equation (9.39) may be integrated immediately to show that the sum of kinetic and potential energy, $u^2/2 + gh$, is constant following the motion. Thus, energy
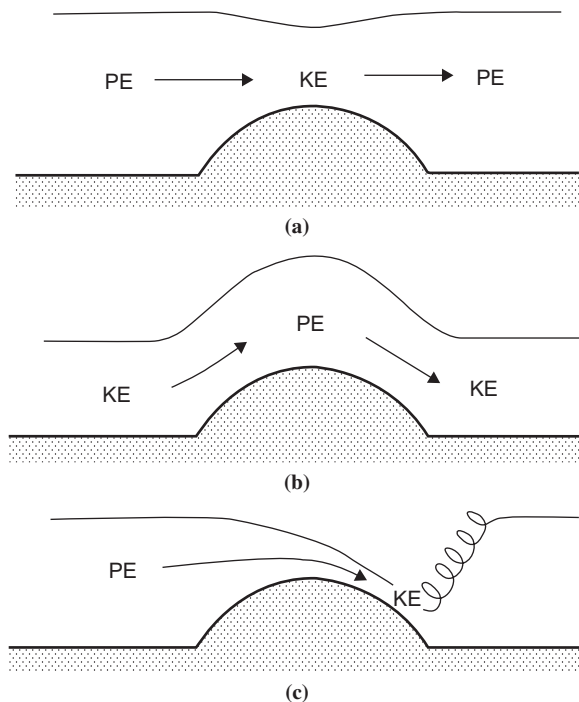
FIGURE 9.10 Flow over an obstacle for a barotropic fluid with free surface. (a) Subcritical flow (Fr > 1 everywhere). (b) Supercritical flow (Fr < 1 everywhere). (c) Supercritical flow on lee slope with adjustment to subcritical flow at hydraulic jump near base of obstacle. (*After Durran, 1990. Copyright © American Meteorological Society. Reprinted with permission.*)

conservation requires that if u increases, h must decrease, and vice versa. In addition, (9.40) shows that the mass flux, $u(h - h_M)$, must also be conserved. The direction of the exchange between kinetic and potential energy in flow over a ridge is determined by the necessity that both (9.39) and (9.40) be satisfied.

Multiplying (9.39) by u and eliminating $\partial h/\partial x$ with the aid of (9.40) gives

$$\left(1 - \text{Fr}^2\right) \frac{\partial u}{\partial x} = \frac{ug}{c^2} \frac{\partial h_M}{\partial x} \tag{9.41}$$

where the shallow water gravity wave speed, c, and the Froude number are now defined using the local thickness and velocity of the fluid:

$$c^2 \equiv g\left(h - h_M\right); \quad \text{Fr}^2 \equiv u^2/c^2$$

From (9.41) it is clear that the flow will accelerate on the upslope side of the ridge ($\partial u/\partial x > 0$, where $\partial h_M/\partial x > 0$) if the Froude number is less than unity, but will decelerate if the Froude number is greater than unity.

As a subcritical flow ascends the upslope side of a topographic barrier, Fr will tend to increase both from the increase in u and the decrease in c. If Fr = 1

at the crest, then from (9.41) the flow will become supercritical and continue to accelerate as it descends the lee side until it adjusts back to the ambient subcritical conditions in a turbulent hydraulic jump as illustrated in Figure 9.10c. In this case very high velocities can occur along the lee slope, as potential energy is converted into kinetic energy during the entire period that a fluid column traverses the barrier. Although conditions in the continuously stratified atmosphere are clearly more complex than in the shallow water hydraulic model, numerical simulations have demonstrated that the hydraulic model provides a reasonable conceptual model for the primary processes occurring in downslope windstorms.

9.5 CUMULUS CONVECTION

Mesoscale storms associated with cumulus convection represent a large fraction of all of the meteorologically important mesoscale circulations. Before considering such systems, it is necessary to examine a few of the essential thermodynamic and dynamical aspects of individual cumulus clouds. The subject of cumulus convection is extremely complex to address theoretically. Much of this difficulty stems from the fact that the cumulus clouds have a complex internal structure. They are generally composed of a number of short-lived individual rising towers, which are produced by elements of ascending buoyant air called *thermals*. Rising thermals *entrain* environmental air and thus modify the cloud air through mixing.

Thermals are nonhydrostatic, nonsteady, and highly turbulent. The buoyancy of an individual thermal (i.e., the difference between its density and the density of the environment) depends on a number of factors, including the environmental lapse rate, the rate of dilution by entrainment, and the drag by the weight of liquid water in cloud droplets. A detailed discussion of the dynamics of thermal convection is beyond the scope of this text. This section utilizes a simple one-dimensional cloud model and focuses primarily on the thermodynamic aspects of moist convection. Convective storm dynamics is considered in Section 9.6.

9.5.1 Convective Available Potential Energy

Development of convective storms depends on the presence of environmental conditions favorable for the occurrence of deep convection. Several indices have been developed to measure the susceptibility of a given temperature and moisture profile to the occurrence of deep convection. A particularly useful measure is the *convective available potential energy*. Convective available potential energy (CAPE) provides a measure of the maximum possible kinetic energy that a statically unstable parcel can acquire (neglecting effects of water vapor and condensed water on the buoyancy), assuming that the parcel ascends

without mixing with the environment and adjusts instantaneously to the local environmental pressure.

The momentum equation for such a parcel is (2.51), which can be rewritten following the vertical motion of the parcel as

$$\frac{Dw}{Dt} = \frac{Dz}{Dt}\frac{Dw}{Dz} = w\frac{Dw}{Dz} = b' \tag{9.42}$$

where $b'(z)$ is again the buoyancy given by

$$b' = g\frac{(\rho_{env} - \rho_{parcel})}{\rho_{parcel}} = g\frac{(T_{parcel} - T_{env})}{T_{env}} \tag{9.43}$$

and T_{env} designates the temperature of the environment. If (9.42) is integrated vertically from the level of free convection, z_{LFC}, to the level of neutral buoyancy, z_{LNB}, following the motion of the parcel the result is

$$\frac{w_{max}^2}{2} = \int_{z_{LFC}}^{z_{LNB}} g\left(\frac{T_{parcel} - T_{env}}{T_{env}}\right) dz \equiv B \tag{9.44}$$

Here, B is the maximum kinetic energy per unit mass that a buoyant parcel can obtain by ascending from a state of rest at the level of free convection to the level of neutral buoyancy near the tropopause (see Figure 2.8). This is an overestimate of the actual kinetic energy realized by a nonentraining parcel, as the negative buoyancy contribution of liquid water reduces the effective buoyancy, especially in the tropics.

In a typical tropical oceanic sounding, parcel temperature excesses of 1 to 2 K may occur over a depth of 10 to 12 km. A typical value of CAPE is then $B \approx 500 \text{ m}^2 \text{ s}^{-2}$. In severe storm conditions in the Midwest of North America, however, parcel temperature excesses can be 7 to 10 K (refer to Figure 2.8) and $B \approx 2000$ to $3000 \text{ m}^2 \text{ s}^{-2}$. Observed updrafts in the latter case (up to 50 m s^{-1}) are much stronger than in the former case (5–10 m s^{-1}). The small value of CAPE in the mean tropical environment is the major reason that updraft velocities in tropical cumulonimbus are observed to be much smaller than those in midlatitude thunderstorms.

9.5.2 Entrainment

In the previous subsection it was assumed that convective cells rise without mixing with environmental air so that they maintain constant θ_e during their rise. In reality, however, rising saturated air parcels tend to be diluted by entraining, or mixing in, some of the relatively dry environmental air. If the air in the environment is unsaturated, some of the liquid water in the rising parcel

must be evaporated to maintain saturation in the convective cell as air from the environment is entrained. The evaporative cooling caused by entrainment will reduce the buoyancy of the convective parcel (i.e., lower its θ_e). Thus, the equivalent potential temperature in an entraining convection cell will decrease with height rather than remaining constant. Similar considerations hold for any other conservable variable[2] in which environmental values differ from cloud values; entrainment will modify the in-cloud vertical profiles.

Denoting as A the amount of an arbitrary conservable variable per unit mass of air, the vertical dependence of A in an entraining convective cell can be estimated by assuming that to a first approximation the cell can be modeled as a steady-state jet as shown in Figure 9.11. Thus, in a time increment δt, a mass m of saturated cloud air with an amount of the arbitrary variable given by mA_{cld} mixes with a mass δm of entrained environmental air, which has an amount of the arbitrary variable given by $\delta m A_{env}$. The change in the value of A within the cloud, δA_{cld}, is then given by the mass balance relationship

$$(m + \delta m)\,(A_{cld} + \delta A_{cld}) = mA_{cld} + \delta m A_{env} + \left(DA_{cld}\big/Dt\right)_S m\delta t \qquad (9.45)$$

where $\left(DA_{cld}\big/Dt\right)_S$ designates the rate of change of A_{cld} due to sources and sinks unrelated to entrainment. Dividing through by δt in (9.45), neglecting the
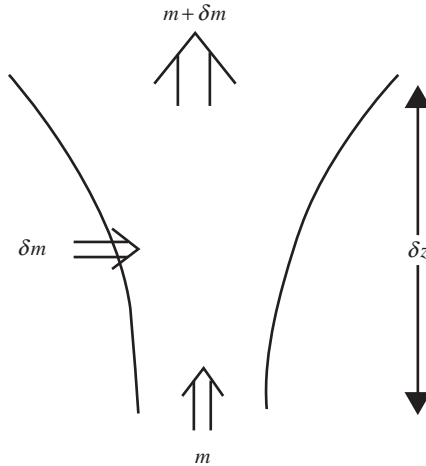
FIGURE 9.11   An entraining jet model of cumulus convection. See text for an explanation.

---

[2]A conservable variable is one that is conserved following the motion in the absence of sources and sinks (e.g., a chemical trace constituent).

second-order term, and rearranging yields

$$\frac{\delta A_{cld}}{\delta t} = \left(\frac{DA_{cld}}{Dt}\right)_S - \frac{1}{m}\frac{\delta m}{\delta t}(A_{cld} - A_{env}) \qquad (9.46)$$

Noting that in the time increment δt an ascending parcel rises a distance $\delta z = w\delta t$, where w is the speed of ascent of the parcel, we can eliminate δt in (9.46) to obtain an equation for the vertical dependence of A_{cld} in a continuously entraining convective cell:

$$w\frac{dA_{cld}}{dz} = \left(\frac{DA_{cld}}{Dt}\right)_S - w\lambda(A_{cld} - A_{env}) \qquad (9.47)$$

where we have defined the *entrainment rate*; $\lambda \equiv d\ln m/dz$.

Letting $A_{cld} = \ln\theta_e$ and noting that θ_e is conserved in the absence of entrainment, (9.47) yields

$$\begin{aligned}
\left(\frac{d\ln\theta_e}{dz}\right)_{cld} &= -\lambda[(\ln\theta_e)_{cld} - (\ln\theta_e)_{env}] \\
&\approx -\lambda\left[\frac{L_c}{c_pT}(q_s - q_{env}) + \ln\left(\frac{T_{cld}}{T_{env}}\right)\right]
\end{aligned} \qquad (9.48)$$

where (2.70) is used to obtain the latter form of the right side. Thus, an entraining convective cell is less buoyant than a nonentraining cell. Letting $A_{cld} = w$ in (9.47), applying (9.42), and neglecting the pressure contribution to buoyancy, we find that the height dependence of kinetic energy per unit mass is given by

$$\frac{d}{dz}\left(\frac{w^2}{2}\right) = g\left(\frac{T_{cld} - T_{env}}{T_{env}}\right) - \lambda w^2 \qquad (9.49)$$

An entraining cell will undergo less acceleration than a nonentraining cell not only because the buoyancy is reduced, but also because of the drag exerted by mass entrainment.

Equations (9.48) and (9.49), together with suitable relations for the cloud moisture variables, can be used to determine the vertical profile of cloud variables. Such one-dimensional cloud models have been very popular in the past. Unfortunately, observed cloud properties, such as maximum cloud depth and cloud water concentration, cannot simultaneously be satisfactorily predicted by this type of model. In reality, pressure perturbations generated by the convective cells are important in the momentum budget, and entrainment does not occur instantaneously but in a sporadic manner that allows some cells to rise through most of the troposphere with very little dilution. Although more sophisticated one-dimensional models can partly overcome these deficiencies, some of the most important aspects of thunderstorm dynamics (e.g., the influence of vertical shear of the environmental wind) can only be included in multidimensional models.

9.6   CONVECTIVE STORMS

Convective storms can take a large variety of forms. These range in scale from isolated thunderstorms involving a single convective cloud (or *cell*) to mesoscale convective complexes consisting of ensembles of multicelled thunderstorms. Here we distinguish three primary types: the single-cell, the multicell, and the supercell storm. As shown in the previous section, convective available potential energy measures whether thermodynamical conditions are favorable for the development of cumulus convection. CAPE, therefore, provides a guide to the strength of convection. It does not, however, provide any notion of the most likely type of mesoscale organization. It turns out, as suggested earlier, that storm type also depends on the vertical shear of the lower tropospheric environment.

When vertical shear is weak (<10 m s^{-1} below 4 km), single cell storms occur. These tend to be short-lived ($\sim$30 min) and move with the mean wind in the lowest 8 km. When there is moderate vertical shear ($\sim$10–20 m s^{-1} below 4 km), multicell storms arise in which individual cells have lifetimes of $\sim$30 min, but the storm lifetime may be many hours. In multicell storms the downdrafts induced by the evaporation of precipitation form a dome of cold outflowing air at the surface. New cells tend to develop along the *gust front* where the cold outflow lifts conditionally unstable surface air. When vertical shear is large (>20 m s^{-1} below 4 km), the strong tilting of convective cells tends to delay storm development, even in a thermodynamically favorable environment, so that an hour or more may be required for the initial cell to completely develop. This development may be followed by a split into two storms, which move to the left and right of the mean wind. Usually the left-moving storm dies rapidly, while the right-moving storm slowly evolves into a rotating circulation with a single updraft core and trailing downdrafts, as discussed in the next section. Such supercell storms often produce heavy rain, hail, and damaging tornadoes. Ensembles of multicell or supercell storms are often organized along lines referred to as *squall lines*, which may move in a different direction than the individual thunderstorms.

9.6.1   Development of Rotation in Supercell Thunderstorms

The supercell thunderstorm is of particular dynamical interest because of its tendency to develop a rotating mesocyclone from an initially nonrotating environment. The dominance of cyclonic rotation in such systems might suggest that the Coriolis force plays a role in supercell dynamics. However, it can be shown readily that the rotation of Earth is not relevant to the development of rotation in supercell storms.

Although a quantitative treatment of supercell dynamics requires that the density stratification of the atmosphere be taken into account, for purposes of understanding the processes that lead to the development of rotation in such

systems and to the dominance of the right-moving cell, it is sufficient to use the Boussinesq approximation. The Euler momentum equation and continuity equation may then be expressed as

$$\frac{D\mathbf{U}}{Dt} = \frac{\partial\mathbf{U}}{\partial t} + (\mathbf{U} \cdot \nabla)\,\mathbf{U} = -\frac{1}{\rho_0}\nabla p + b\mathbf{k}$$

$$\nabla \cdot \mathbf{U} = 0$$

Here, $\mathbf{U} \equiv \mathbf{V} + \mathbf{k}w$ is the three-dimensional velocity, ∇ is the three-dimensional del operator, ρ_0 is the constant basic state density, p is the deviation of pressure from its horizontal mean, and $b \equiv -g\rho'/\rho_0$ is the total buoyancy.

It is convenient to rewrite the momentum equation using the vector identity

$$(\mathbf{U} \cdot \nabla)\,\mathbf{U} = \nabla\left(\frac{\mathbf{U} \cdot \mathbf{U}}{2}\right) - \mathbf{U} \times (\nabla \times \mathbf{U})$$

to obtain

$$\frac{\partial\mathbf{U}}{\partial t} = -\nabla\left(\frac{p}{\rho_0} + \frac{\mathbf{U} \cdot \mathbf{U}}{2}\right) + \mathbf{U} \times \boldsymbol{\omega} + b\mathbf{k} \qquad (9.50)$$

Taking $\nabla \times$ (9.50) and recalling that the curl of the gradient vanishes, we obtain the three-dimensional vorticity equation

$$\frac{\partial\boldsymbol{\omega}}{\partial t} = \nabla \times (\mathbf{U} \times \boldsymbol{\omega}) + \nabla \times (b\mathbf{k}) \qquad (9.51)$$

Letting $\zeta = \mathbf{k} \cdot \boldsymbol{\omega}$ be the vertical component of vorticity and taking $\mathbf{k}\cdot$ (9.51), we obtain an equation for the tendency of ζ in a nonrotating reference frame:

$$\frac{\partial\zeta}{\partial t} = \mathbf{k} \cdot \nabla \times (\mathbf{U} \times \boldsymbol{\omega}) \qquad (9.52)$$

Note that buoyancy only affects the horizontal vorticity components.

We now consider a flow consisting of a single convective updraft embedded in a basic state westerly flow that depends on z alone. Linearizing about this basic state by letting

$$\boldsymbol{\omega} = \mathbf{j}d\bar{u}/dz + \boldsymbol{\omega}'\,(x, y, z, t), \quad \mathbf{U} = \mathbf{i}\bar{u} + \mathbf{U}'\,(x, y, z, t)$$

and noting that the linearized form of the right side in (9.52) becomes

$$\mathbf{k} \cdot \nabla \times (\mathbf{U} \times \boldsymbol{\omega}) = -\mathbf{k} \cdot \nabla \times \left(\mathbf{i}w'd\bar{u}/dz + \mathbf{j}\bar{u}\zeta'\right)$$

we find that the linearized vorticity tendency is

$$\frac{\partial\zeta'}{\partial t} = -\bar{u}\frac{\partial\zeta'}{\partial x} + \frac{\partial w'}{\partial y}\frac{d\bar{u}}{dz} \qquad (9.53)$$

The first term on the right in (9.53) is just the advection by the basic state flow. The second term represents tilting of horizontal shear vorticity into the vertical by differential vertical motion.

Because $d\bar{u}/dz$ is positive, the vorticity tendency due to this tilting will be positive to the south of the updraft core and negative to the north of the updraft core. As a result, a counterrotating vortex pair is established with cyclonic rotation to the south and anticyclonic rotation to the north of the initial updraft, as shown in Figure 9.12a. Eventually, the development of negative buoyancy due to precipitation loading generates an upper-level downdraft at the position of the initial updraft, and the storm splits as shown in Figure 9.12b. New updraft cores are established centered on the counterrotating vortex pair.

To understand the generation of updrafts in the vortices on the flanks of the storm, we examine the perturbation pressure field. A diagnostic equation for the disturbance pressure is obtained by taking $\nabla \cdot$ (9.53) to yield

$$\nabla^2 \left(\frac{p}{\rho_0} \right) = -\nabla^2 \left(\frac{\mathbf{U} \cdot \mathbf{U}}{2} \right) + \nabla \cdot (\mathbf{U} \times \boldsymbol{\omega}) + \frac{\partial b}{\partial z} \qquad (9.54)$$

The first two terms on the right in (9.54) represent dynamical forcing, whereas the last term represents buoyancy forcing. Observations and numerical models suggest that the buoyancy forcing in (9.54) produces pressure perturbations that tend partly to compensate for the buoyancy force in the vertical momentum equation. Dynamically forced pressure perturbations, however, may generate substantial vertical accelerations.

To compute the dynamical contribution to the disturbance pressure gradient force in either the right or left vortex, we use cylindrical coordinates (r, λ, z) centered on the axis of rotation of either vortex, and assume that to a first approximation the azimuthal velocity v_λ (positive for cyclonic flow) is independent of λ. In this system the storm relative horizontal motion and vertical component of vorticity are given approximately by
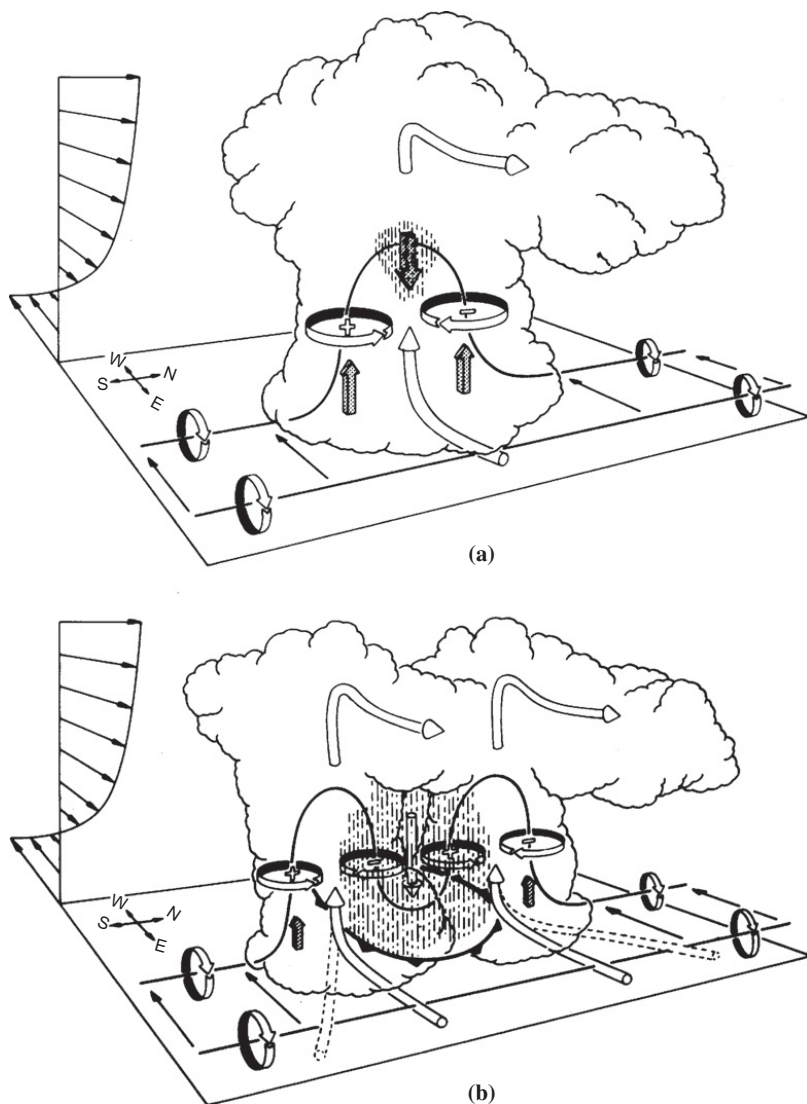
$$\mathbf{U}' \approx \mathbf{j}_\lambda v_\lambda, \quad \mathbf{k} \cdot \boldsymbol{\omega}' = \zeta' \approx r^{-1} \partial (r v_\lambda) / \partial r$$

where $\mathbf{j}_\lambda$ is the unit vector in the azimuthal direction (positive counterclockwise) and r is the distance from the axis of the vortex. Letting $\mathbf{i}_\lambda$ be the unit vector in the radial direction, we then have

$$\mathbf{U} \times \boldsymbol{\omega} \approx \mathbf{i}_\lambda \frac{v_\lambda}{r} \frac{\partial}{\partial r} (r v_\lambda)$$

Assuming that the vertical scale is much larger than the radial scale, the Laplacian in cylindrical coordinates can be approximated by

$$\nabla^2 \approx \frac{1}{r} \frac{\partial}{\partial r} \left(r \frac{\partial}{\partial r} \right)$$

FIGURE 9.12 Development of rotation and splitting in a supercell storm with westerly mean wind shear (shown by storm relative wind *arrows* in the *upper left* corner of each panel). *Cylindrical arrows* show the direction of cloud relative air flow. *Heavy solid lines* show vortex lines with a sense of rotation shown by *circular arrows*. *Plus and minus signs* indicate cyclonic and anticyclonic rotation caused by vortex tube tilting. *Shaded arrows* represent updraft and downdraft growth. *Vertical dashed lines* denote regions of precipitation. (a) In the initial stage, the environmental shear vorticity is tilted and stretched into the vertical as it is swept into the updraft. (b) In the splitting stage, downdraft forms between the new updraft cells. The *arced line* with triangles in the lower middle of (b) at the surface indicates downdraft outflow at the surface. (*After Klemp, 1987. Used with permission from Annual Reviews.*)

Thus, from (9.54) the dynamical component of the pressure perturbation in the vortices (designated p_{dyn}) can be expressed as

$$\frac{1}{r}\frac{\partial}{\partial r}\left(\frac{r}{\rho_0}\frac{\partial p_{dyn}}{\partial r}\right) \approx -\frac{1}{r}\frac{\partial}{\partial r}\left[r\frac{\partial\left(v_\lambda^2/2\right)}{\partial r}\right] + \frac{1}{r}\frac{\partial}{\partial r}\left[v_\lambda\frac{\partial\left(rv_\lambda\right)}{\partial r}\right] = \frac{1}{r}\frac{\partial v_\lambda^2}{\partial r}$$

(9.55)

Integrating (9.55) with respect to r, we obtain the equation of cyclostrophic balance (see Section 3.2.4):

$$\rho_0^{-1}\partial p_{dyn}\big/\partial r \approx v_\lambda^2/r \tag{9.56}$$

Hence, there is a pressure minimum at the vortex center irrespective of whether the rotation is cyclonic or anticyclonic. The strong midtropospheric rotation induced by vortex tube twisting and stretching creates a "centrifugal pump" effect, which causes a negative dynamical pressure perturbation centered in the vortices in the midtroposphere. This in turn produces an upward-directed dynamical contribution to the vertical component of the pressure gradient force, and thus provides an upward acceleration, which produces updrafts in the cores of the counterrotating vortices as depicted in Figure 9.12. These updrafts are separated by a downdraft that leads to a splitting of the storm and the development of two new centers of convection that move to the right and left of the original storm (Figure 9.12b).

   As discussed in this section, the tilting and stretching of horizontal vorticity associated with the vertical shear of the basic state wind can account for the development of mesoscale rotating supercells. This process does not, however, appear to be able to produce the large vorticities observed in the tornadoes that often accompany supercell thunderstorms. Numerical simulations suggest that these tend to involve tilting and stretching of especially strong horizontal vorticity produced by horizontal gradients in buoyancy that occur near the surface along the *gust front* where negatively buoyant outdrafts produced by convective downdrafts meet moist, warm boundary layer air.

9.6.2   The Right-Moving Storm

When the environmental wind shear is unidirectional, as in the case discussed previously (see also Figure 9.13a), the anticyclonic (left-moving) and cyclonic (right-moving) updraft cores are equally favored. In most severe storms in the central United States, however, the mean flow turns anticyclonically with height; this directional shear in the environment favors the right-moving storm center, while inhibiting the left-moving center. Thus, right-moving storms are observed far more than left-moving storms.

   The dominance of the right-moving storm can be understood qualitatively by again considering the dynamical pressure perturbations. We define the basic state wind shear vector $\overline{\mathbf{S}} \equiv \partial\overline{\mathbf{V}}\big/\partial z$, which is assumed to turn clockwise with
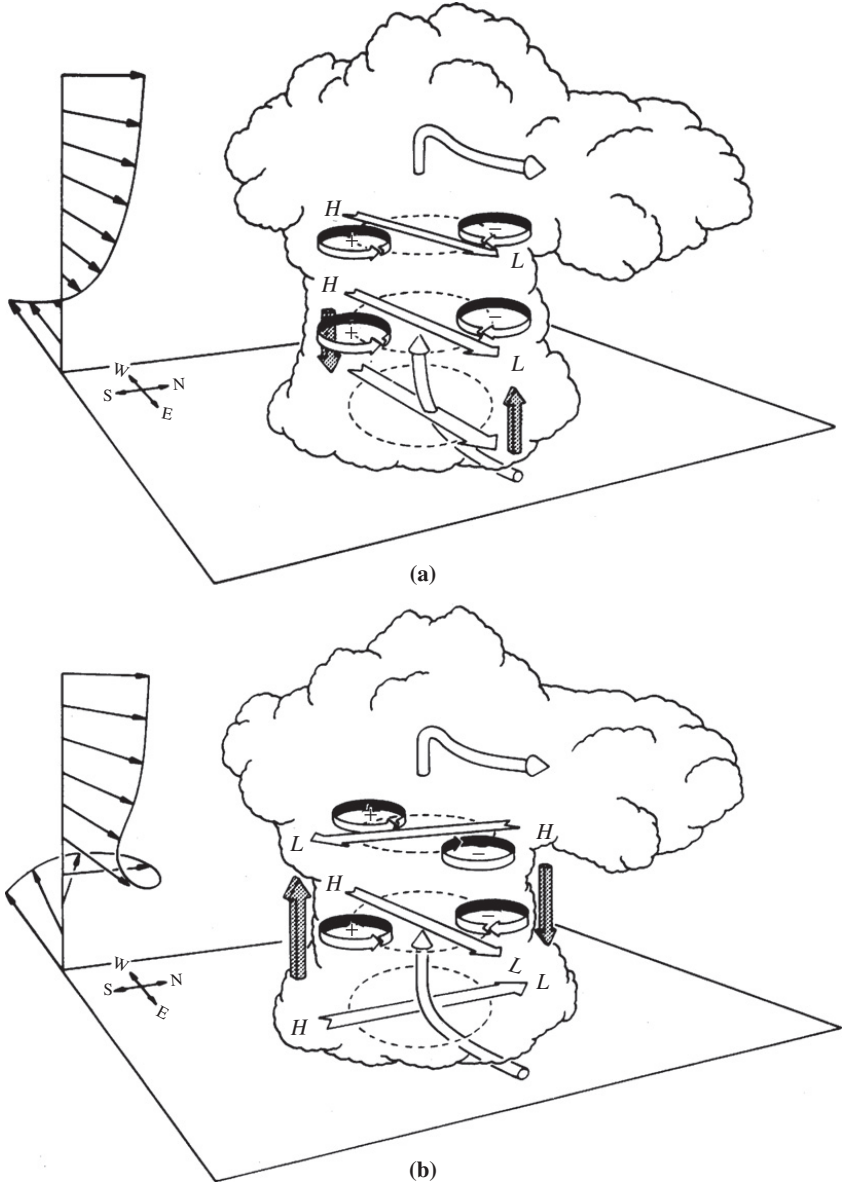
FIGURE 9.13 Pressure and vertical vorticity perturbations produced by interaction of the updraft with environmental wind shear in a supercell storm. (a) Wind shear does not change direction with height. (b) Wind shear turns clockwise with height. *Broad open arrows* designate the shear vectors. *H* and *L* designate high and low dynamical pressure perturbations, respectively. *Shaded arrows* show resulting disturbance vertical pressure gradients. (*After Klemp, 1987. Used with permission from Annual Reviews.*)

height. Noting that the basic state horizontal vorticity in this case is

$$\overline{\boldsymbol{\omega}} = \mathbf{k} \times \overline{\mathbf{S}} = -\mathbf{i}\partial\overline{v}/\partial z + \mathbf{j}\partial\overline{u}/\partial z$$

we see that there is a contribution to the dynamic pressure in (9.54) of the form

$$\nabla \cdot \left(\mathbf{U}' \times \overline{\boldsymbol{\omega}}\right) \approx -\nabla \cdot \left(w'\overline{\mathbf{S}}\right)$$

From (9.54) the sign of the pressure perturbation due to this effect may be determined by noting that

$$\nabla^2 p_{dyn} \sim -p_{dyn} \sim -\frac{\partial}{\partial x}\left(w'S_x\right) - \frac{\partial}{\partial y}\left(w'S_y\right) \tag{9.57}$$

which shows that there is a positive dynamical pressure perturbation upshear of the cell and a negative perturbation pressure downshear (analogous to the positive pressure perturbation upwind and negative perturbation downwind of an obstacle). The resulting pattern of dynamical pressure perturbations is shown in Figure 9.13. In the case of unidirectional shear (Figure 9.13a), the induced pressure pattern favors updraft growth on the leading edge of the storm. However, when the shear vector rotates clockwise with height as in Figure 9.13b, (9.57) shows that a dynamical pressure disturbance pattern is induced in which there is an upward-directed vertical pressure gradient force on the flank of the cyclonically rotating cell and a downward-directed pressure gradient force on the flank of the anticyclonic cell. Thus, in the presence of clockwise rotation of the environmental shear, stronger updrafts are favored in the right-moving cyclonic vortex to the south of the initial updraft.
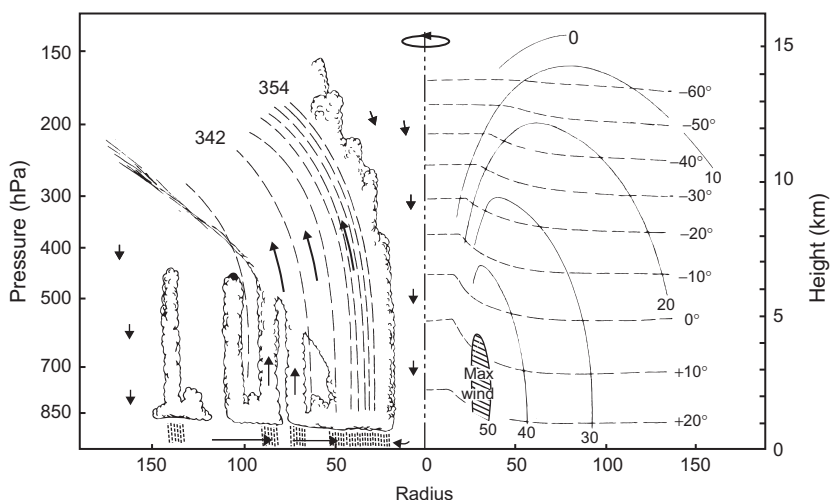
9.7 HURRICANES

Hurricanes, which are also referred to as tropical cyclones and typhoons in some parts of the world, are intense vortical storms that develop over the tropical oceans in regions of very warm surface water. Although the winds and convective clouds observed in hurricanes are not truly axisymmetric about the vortex center, the fundamental aspects of hurricane dynamics can be modeled by idealizing the hurricane as an axisymmetric vortex. Typically hurricanes have radial scales of several hundred kilometers, similar to those of some midlatitude synoptic systems. However, the horizontal scale of the region of intense convection and strong winds in a hurricane is typically only about 100 km in radius. Thus, it is reasonable to classify hurricanes as mesoscale systems.

Unlike the rotating convective storms treated in the previous section, the hurricane vortex cannot be understood without including the rotation of Earth in the vorticity balance. The rapid rotation observed in hurricanes is produced by concentration of the vertical component of absolute vorticity by vortex stretching, not by tilting horizontal vorticity into the vertical. Maximum tangential

wind speeds in these storms range typically from 50 to 100 m s^{-1}. For such high velocities and relatively small scales, the centrifugal force term cannot be neglected compared to the Coriolis force. Thus, to a first approximation, the azimuthal velocity in a steady-state hurricane is in gradient wind balance with the radial pressure gradient force. Hydrostatic balance also holds on the hurricane scale, which implies that the vertical shear of the azimuthal velocity is a function of the radial temperature gradient.

The hurricane *primary circulation* consists of cyclonic flow around a center of low pressure, with the maximum wind located roughly 15 to 50 km from the center and about 1 to 1.5 km altitude, near the top of the boundary layer (Figure 9.14). The hurricane *secondary circulation* consists of radial inflow at low levels, which rises in the eyewall while conserving equivalent potential temperature, and then moves radially away from the storm at upper levels in the outflow layer before gradually subsiding in the surrounding environment. This secondary circulation is driven by radial gradients of latent heating in the eyewall and vertical gradients of momentum dissipation in the boundary layer; it may be understood through a generalization of (9.15) to include these effects. Within the eyewall the θ_e and angular momentum surfaces coincide, so parcel ascent in the eyewall is neutral with respect to conditional symmetric instability and thus does not require external forcing. The eyewall surrounds a central eye

FIGURE 9.14   Schematic illustration of hurricane structure. *Thin solid curves* show the azimuthal wind speeds, which peak in the lower troposphere. Mainly *horizontal dashed lines* give the temperature field, which reflects the decrease with height in the troposphere. Mainly *vertical thin dashed lines* show equivalent potential temperature, which is well mixed in the eyewall. *Arrows* denote the secondary circulation, with radial inflow at low levels, ascent in the eyewall, and subsidence in the environment and inside the eye. (*Adapted from Wallace and Hobbs, 2006.*)

of radius 15 to 50 km where subsidence occurs, resulting in relatively warm air that is cloud-free above the boundary layer.

9.7.1 Dynamics of Mature Hurricanes

Because of the fact that tropical cyclones are primarily axisymmetric and have well-defined centers, angular momentum is a useful measure of storm intensity. Angular momentum about the vertical axis is defined by

$$m = rv + fr^2 \qquad (9.58)$$

The azimuthal gradient wind, V, in pressure coordinates is determined by

$$\frac{\partial \Phi}{\partial r} = \frac{V^2}{r} + fV \qquad (9.59)$$

and hydrostatic balance in terms of the specific volume, α, is determined by

$$\frac{\partial \Phi}{\partial p} = -\alpha \qquad (9.60)$$

A thermal wind equation is obtained by equating $\partial/\partial p$ (9.59) and $\partial/\partial r$ (9.60), giving

$$-\frac{\partial \alpha}{\partial r} = \frac{2m}{r^3}\frac{\partial m}{\partial p} \qquad (9.61)$$

Although this form of the thermal wind equation is different than the one discussed in Chapter 3, the general interpretation is similar: Radial gradients in density are linked to vertical gradients in angular momentum. Specific volume may be eliminated from (9.61) in favor of entropy using so-called Maxwell relations[3]:

$$\left.\frac{\partial \alpha}{\partial r}\right|_p = \frac{\partial \alpha}{\partial s}\frac{\partial s}{\partial r}$$

$$\left.\frac{\partial \alpha}{\partial s}\right|_p = \left.\frac{\partial T}{\partial p}\right|_s \qquad (9.62)$$

Since entropy and angular momentum contours are, to good approximation, congruent in the eyewall, we take entropy to be a function of angular momentum alone. This implies that radial entropy gradients are proportional to radial

---

[3]Wikipedia has a particularly good description of these relationships among thermodynamic variables, which result from constraints in the First Law of Thermodynamics and commutation of partial derivatives.

angular momentum gradients:

$$\frac{\partial s}{\partial r}\bigg|_p = \frac{\partial s}{\partial m}\frac{\partial m}{\partial r} \tag{9.63}$$

so that (9.61) becomes

$$\frac{2m}{r^3}\frac{\partial m}{\partial p} = -\frac{\partial T}{\partial p}\bigg|_s \frac{\partial s}{\partial m}\frac{\partial m}{\partial r} \tag{9.64}$$

Alternatively, noting that

$$\frac{\partial m/\partial p}{\partial m/\partial r} = -\frac{\partial r}{\partial p}\bigg|_m \tag{9.65}$$

thermal wind can be expressed in terms of the slope of angular momentum (and entropy) surfaces

$$\frac{2m}{r^3}\frac{\partial r}{\partial p}\bigg|_m = -\frac{\partial T}{\partial p}\bigg|_s \frac{\partial s}{\partial m} \tag{9.66}$$

Although (9.66) applies at each level in the eyewall, it proves useful to integrate this equation along the angular momentum surface that extends from the point of maximum wind above the boundary layer, **b**, to a point in the outflow, **t**, (Figure 9.15). Integration over the interval yields

$$\frac{1}{r_b^2} - \frac{1}{r_t^2} = \frac{1}{m}\frac{\partial s}{\partial m}(T_t - T_b) \tag{9.67}$$

Assuming that the outflow radius is much larger than the radius of maximum wind, the second left-side term may be neglected, which reveals that angular momentum depends on the radius of maximum wind, r_b, as anticipated by (9.58), the temperature difference between point of maximum wind and the outflow, and the relationship between entropy and angular momentum. This last relationship is determined by the following closure scheme for the boundary layer. If the dominant balance in the entropy and angular momentum equations in the boundary layer is between radial advection and turbulent mixing, then

$$\begin{aligned}
-u\frac{\partial m}{\partial r} &\approx \frac{\partial \tau_m}{\partial z}\\
-u\frac{\partial s}{\partial r} &\approx \frac{\partial \tau_s}{\partial z}
\end{aligned} \tag{9.68}$$
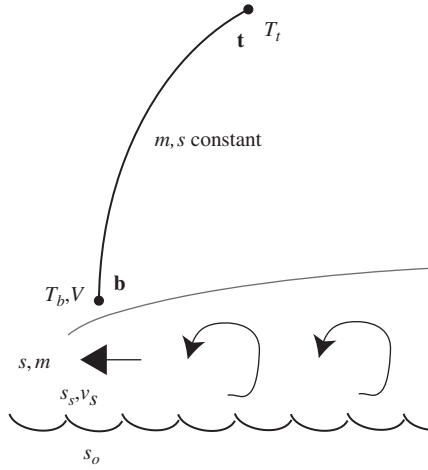
FIGURE 9.15   Essential elements of the potential intensity theory. The *bold curve* with endpoints **b** and **t** denotes the constant entropy and angular momentum surface along which the thermal wind equation is integrated. The curve originates at the top of the boundary layer, which is denoted by the *sloping gray curve*. Within the boundary layer, radial advection of entropy and angular momentum, denoted by the *bold arrow* (positive for angular momentum and negative for entropy) is balanced by vertical flux divergence due to turbulence, denoted by the *curved arrows*. At the sea surface, there exists an entropy difference between values in the atmosphere, s_s and ocean, s_o. The surface wind speed is given by v_s.

where τ_m and τ_s are the vertical turbulent fluxes (see Section 8.3) of angular momentum and entropy, respectively. Dividing these equations indicates

$$\left.\frac{\partial s}{\partial m}\right|_r = \left.\frac{\partial \tau_s}{\partial \tau_m}\right|_z \tag{9.69}$$

which indicates that the relationship between entropy and angular momentum is controlled by the relationship between the turbulent fluxes. We now assume that these turbulent fluxes are independent of depth in the boundary layer, so they may be determined from surface fluxes, which are given by aerodynamic formulae (Section 8.3.1):

$$\begin{aligned} \tau_{s0} &= C_S |\mathbf{V}|_0 (s_s - s_o) \\ \tau_{m0} &= C_D |\mathbf{V}|_0 (m_s - m_o) = C_D |\mathbf{V}|_0 r v_s \end{aligned} \tag{9.70}$$

Here, $|\mathbf{V}|_0$ is the surface wind speed, and C_S and C_D are the surface exchange coefficients for entropy and angular momentum, respectively. The surface value of entropy (angular momentum) for the atmosphere is given by s_s (m_s), and analogously, for the surface of the ocean, we have s_o and m_o. In the last equality for the angular momentum flux we assumed that the azimuthal speed of the ocean is small compared to the atmosphere, v_s. Note that no assumption has been made about the azimuthal wind in the boundary layer; in particular, the wind is not

assumed to be in gradient wind balance. Combining equations (9.70) gives

$$\tau_{s0} = \left[\frac{C_S(s_s - s_o)}{C_D r v_s} \right] \tau_{m0} \tag{9.71}$$

which from (9.69) immediately recovers

$$\left. \frac{\partial s}{\partial m} \right|_r = \frac{C_S(s_s - s_o)}{C_D r v_s} \tag{9.72}$$

Armed with the relationship between entropy and angular momentum, we return to (9.67) and use (9.72) assuming large r_t to yield

$$\frac{m v_s}{r_b} = \frac{C_S}{C_D}(s_o - s_s)(T_b - T_t) \tag{9.73}$$

Using (9.58) indicates that the left side of (9.73) is equal to

$$V v_s + 0.5 f r_b v_s \tag{9.74}$$

For typical hurricane parameters the second term may be neglected within approximately 5% error. Finally, we use a "surface wind reduction factor" to relate the gradient wind at the point of maximum wind, V, to the windspeed at the ocean surface (not a gradient wind), $v_s = aV$; observations indicate that the value of a is often around 0.8 to 0.9. These substitutions yield the "potential intensity" formula for a steady-state storm (Emanuel, 1988)

$$\boxed{V^2 = a^{-1} \frac{C_S}{C_D}(s_o - s_s)(T_b - T_t)} \tag{9.75}$$

Aside from the factor a, which has about a 5% effect, we see that steady-state hurricane intensity depends on the square root of the ratio of the surface exchange coefficients, the surface entropy difference between ocean and atmosphere, and the temperature difference between the top of the boundary layer and the outflow. The ratio of surface exchange coefficients is not known exactly, but is thought to be around 0.7. The surface entropy difference is due to a combination of moisture and thermal effects, with a net flux of both quantities from the ocean to the atmosphere. Therefore, although it may seem counterintuitive, (9.75) indicates that the potential intensity *in steady state* is higher when the atmosphere is colder and drier; the physical reason is that such situations promote the development of larger radial gradients of entropy. Although T_b applies at the top of the boundary layer, it is commonly approximated by the sea-surface temperature, which allows one to create global maps estimating the potential intensity of storms that form in these areas.

Since (9.75) estimates steady-state intensity, it does not apply to short-term intensity fluctuations. As such, one may expect to find storms that occasionally exceed (9.75), even when all assumptions are well satisfied; nevertheless, the time average over these transient periods should be limited by (9.75). Of course,
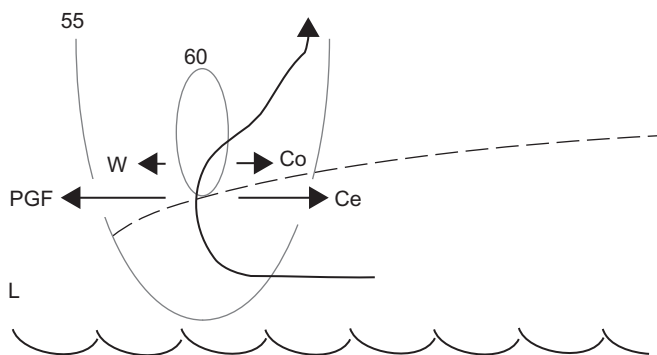
FIGURE 9.16 Illustration of unbalanced contributions to the azimuthal wind following an air parcel from the boundary layer into the free atmosphere (*thick arrow*) near the radius of maximum wind (isotachs of azimuthal wind speed given by *gray contours* in m/s). A large pressure gradient force is directed inward toward low pressure in the eye ("**L**"). If vertical motion is small, then the vertical advection of horizontal azimuthal momentum ("W") may be neglected, which results in a balance between the pressure gradient force and the sum of the Coriolis ("Co") and centrifugal ("Ce") forces—that is, gradient wind balance. If vertical advection is large, a stronger azimuthal wind is required to achieve balance, which yields winds stronger than that for gradient balance. In this situation, when parcels approach the level maximum wind, vertical advection approaches zero, resulting in a net outward force that decelerates the wind.

if the assumptions behind (9.75) fail, then the estimate will as well. One aspect where this may occur fairly often is in the gradient wind assumption at the point of maximum wind. Specifically, vertical advection of azimuthal momentum in the boundary layer introduces an extra term in the momentum equation not considered by gradient wind balance. Below the level of maximum wind, the contribution from this term is of the same sign as the pressure gradient force (Figure 9.16). In steady state, the centrifugal and Coriolis forces required to balance these effects are larger than in the absence of vertical advection. As a result, the azimuthal wind tends to be supergradient near the top of the boundary layer, and this effect can become large if vertical advection is also large, which happens when the radial gradient of radial wind is large. As air parcels approach the level of maximum wind, vertical advection approaches zero, resulting in a net outward force that decelerates the air parcel. As a result, air tends to flow radially outward just above the boundary layer, particularly in cases when the supergradient effect is large.

9.7.2 Hurricane Development

The origin of tropical cyclones is still a matter of active research. Although there are many tropical disturbances each year, only rarely does one develop into a hurricane. Thus, the development of a hurricane requires rather special conditions. As shown in Chapter 7, linear stability theory is quite successful in accounting for the development of extratropical baroclinic disturbances. As

such, this approach provides a reasonable starting point for theoretical investigations of hurricane development, where one seeks the conditions under which unstable amplification of an initial disturbance can occur.

In the tropics, however, the only well-documented linear instability is conditional instability. This instability has its maximum growth rate on the scale of an individual cumulus cloud. Therefore, it cannot explain the synoptic-scale organization of the motion. Observations indicate, moreover, that the mean tropical atmosphere is not saturated, even in the planetary boundary layer. Thus, a parcel must undergo a considerable amount of forced ascent before it reaches its LFC and becomes positively buoyant. Such forced parcel ascent can only be caused by small-scale motions, such as turbulent plumes in the boundary layer. The efficacy of boundary layer turbulence in producing parcel ascent to the LFC clearly depends on the temperature and humidity of the boundary layer environment. In the tropics it is difficult to initialize deep convection unless the boundary layer is brought toward saturation and destabilized, which may occur if there is large-scale (or mesoscale) ascent in the boundary layer. Thus, convection tends to be concentrated in regions of large-scale low-level convergence. This concentration does not arise because the large-scale convergence directly "forces" the convection, but rather because it preconditions the environment to be favorable to parcel ascent to the LFC.

Cumulus convection and the large-scale environmental motion are thus often viewed as cooperatively interacting. In this viewpoint, diabatic heating due to latent heat released by cumulus clouds produces a large-scale (or mesoscale) cyclonic disturbance; this disturbance, in turn, through boundary layer pumping, drives the low-level moisture convergence necessary to maintain an environment favorable to the development of cumulus convection. There have been attempts to formalize these ideas into a linear stability theory; this is often referred to as *conditional instability of the second kind* (CISK), which attributes hurricane growth to the organized interaction between the cumulus-scale and the large-scale moisture convergence. This interaction process is indicated schematically in Figure 9.17a. The CISK model for hurricane development has not been successful because there is little evidence that such interaction leads to a growth rate maximum on the observed scale of hurricanes.

A different view of the stability of the tropical atmosphere, referred to as *wind-induced surface heat exchange* (WISHE), is based on air–sea interactions. According to the WISHE view, illustrated schematically in Figure 9.17b, the potential energy for hurricanes arises from the thermodynamic disequilibrium between the atmosphere and the underlying ocean, which is quantified through the entropy difference in (9.75). The efficacy of air–sea interaction in providing potential energy to balance frictional dissipation depends on the rate of transfer of latent heat from the ocean to the atmosphere. This is a function of surface wind speed; strong surface winds, which produce a rough sea surface, can increase the evaporation rate greatly. Thus, hurricane development is enhanced by the presence of a finite-amplitude initiating disturbance, such as an equatorial wave, to provide the winds required to produce strong evaporation. Given

(a)

(b)
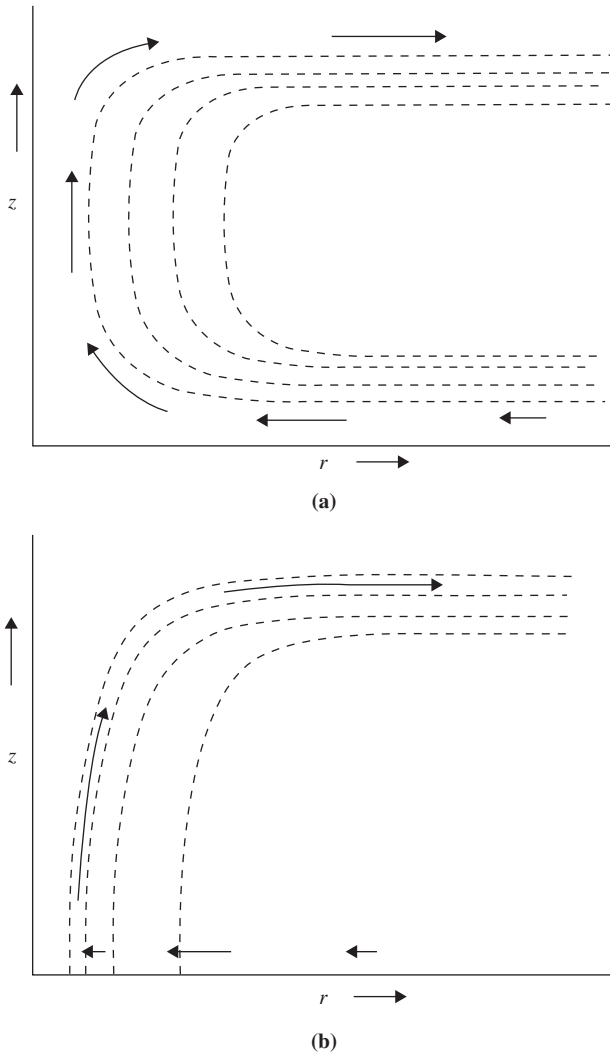
FIGURE 9.17   Meridional cross-sections showing the relationship between surfaces of constant saturation θ_e (*dashed contours*; values decreasing as *r* increases) and meridional circulation (*arrows*) in CISK (a) and WISHE (b) theories for hurricane development. (a) Frictionally induced boundary layer convergence moistens the environment and destabilizes it through layer ascent. This enables small-scale plumes to reach their levels of free convection easily and to produce cumulonimbus clouds. Diabatic heating due to the resulting precipitation drives large-scale circulation and thus maintains the large-scale convergence. (b) The saturation θ_e is tied to the θ_e of the boundary layer. The warm core occurs because enhanced surface fluxes of latent heat increase θ_e there. (*After Emanuel, 2000.*)

a suitable initial disturbance, a feedback may occur in which an increase in inward-spiraling surface winds increases the rate of moisture transfer from the ocean, which increases the intensity of the convection, which further increases the secondary circulation. While it appears that observed cases of tropical cyclogenesis require finite-amplitude initial disturbances, the reason is likely that such disturbances require a shorter period of time to reach maturity. As initial disturbance amplitude decreases, the time required to reach maturity increases, as does the probability of adverse environmental factors disrupting the process.

Many environmental factors may slow or hinder the development process, but the most important are vertical wind shear and dry air. Vertical shear "tilts" the convection so that the heating is not vertically aligned. Moreover, shear produces a dipole of vertical motion about the nascent disturbance, which disturbs the circulation from axisymmetry and results in dry air in the midtroposphere on the upshear side of the storm. Dry air may be entrained into the convection, resulting in strong downdrafts that transport low-entropy air to the surface, reducing conditional instability. Thus, storm development can be substantially inhibited if dry air is continually transported into the midtroposphere above the developing storm. As a result, developing systems that have a deep layer with closed streamlines in a framework moving with the disturbance are favored, since the air is trapped within the disturbance, and convection may moisten the troposphere through detrainment without being replaced by drier environmental air.

SUGGESTED REFERENCES

Durran (1990) reviews the dynamics of mountain waves and downslope windstorms.

Eliassen (1990) discusses the secondary circulation within frontal zones.

Emanuel's *Atmospheric Convection* is a graduate-level text covering the subject of convection, including symmetric instability, in great detail.

Emanuel (2000) provides a qualitative explanation of the WISHE theory for hurricane development.

Keppert and Wang (2001) discuss the importance of vertical advection in generating supergradient winds in tropical cyclone boundary layers.

Hoskins (1982) discusses the semigeostrophic theory of frontogenesis and summarizes results from numerical models.

Houze's *Cloud Dynamics* discusses convective storms at the graduate level.

Klemp (1987) describes the dynamics of tornadic thunderstorms.

PROBLEMS

9.1. Show by transforming from θ coordinates to height coordinates that the Ertel potential vorticity P is proportional to $F^2 N_s^2 - S^4$. See (9.27).

9.2. Starting with the linearized Boussinesq equations for a basic state zonal flow that is a function of height, derive (9.35) and verify the form given for the Scorer parameter.

9.3. Show that for stationary flow over an isolated ridge in the broad ridge limit
($k_s \ll m_s$), the group velocity vector is directed upward so that energy cannot
propagate upstream or downstream of the ridge.

9.4. An air parcel at 920 hPa with temperature 20°C is saturated (mixing ratio
16 g kg^{-1}). Compute θ_e for the parcel.

9.5. Suppose that the mass of air in an entraining cumulus updraft increases
exponentially with height so that $m = m_0 e^{z/H}$, where $H = 8$ km and m_0 is
the mass at a reference level. If the updraft speed is 3 m s^{-1} at 2-km height,
what is its value at a height of 8 km, assuming that the updraft has zero net
buoyancy?

9.6. Verify the approximate relationship between moist static energy and θ_e
given by equation (2.71).

9.7. The azimuthal velocity component in some hurricanes is observed to have
a radial dependence given by $v_\lambda = V_0 (r_0/r)^2$ for distances from the center
given by $r \geq r_0$. Letting $V_0 = 50$ m s^{-1} and $r_0 = 50$ km, find the total
geopotential difference between the far field ($r \to \infty$) and $r = r_0$, assuming
gradient wind balance and $f_0 = 5 \times 10^{-5}$ s^{-1}. At what distance from the
center does the Coriolis force equal the centrifugal force?

9.8. Starting with equation (9.59), derive the angular momentum form of the
gradient wind balance for an axisymmetric vortex given by equation (9.61).

MATLAB Exercises

M9.1. The MATLAB script **surface_front_1.m** demonstrates the concentration of an
initial temperature gradient by an imposed deformation field. The tempera-
ture field is initially taken to have a linear decrease in y: $T(y) = 300 - 10^{-2}y$,
where y is in kilometers. The horizontal wind is given by the streamfunction
$\psi(x, y) = -15k^{-1} \sin(kx) \sin(my)$, where $k = 2\pi/3 \times 10^6$ and $m = \pi/3 \times 10^6$.
Evaluate and contour-plot the deformation field for this streamfunction,
where deformation is defined as $\partial u/\partial x - \partial v/\partial y$. Run the model and observe
where the temperature gradient increases. Modify the code to plot the max-
imum temperature gradient as a function of time. For how long does the
gradient increase approximately exponentially? What is the e-folding time
for increase of the temperature gradient at the origin?

M9.2. The MATLAB script **profile_1.m** and the function **Tmoist.m** use pressure, tem-
perature, and humidity data in the file **sounding.dat** to calculate and graph
vertical profiles of temperature, dewpoint, and the temperature correspond-
ing to pseudoadiabatic ascent from the lifting condensation level for a parcel
lifted from the lowest level of the sounding. Modify this script to plot pro-
files of the potential temperature, the equivalent potential temperature, and
the saturated potential temperature. *Hint:* Temperature at saturation can be
calculated by inverting the expression for saturation vapor pressure, which is
obtainable by integrating equation (D.4):

$$e_s = e_{s,tr} \exp \left[\frac{L_v}{R_v} \left(\frac{1}{T_{tr}} - \frac{1}{T} \right) \right]$$

where $e_{s,tr} = 6.11$ hPa, $T_{tr} = 273.16$ K, and $L_v = 2.5 \times 10^6$ J kg^{-1} are the
saturation vapor pressure at the triple point temperature, the triple point
temperature, and the latent heat of vaporization, respectively.

M9.3. For the thermodynamic sounding of Problem M9.2, compute the CAPE and the profile of vertical velocity for a parcel lifted from the lowest layer in the absence of entrainment. What is the maximum vertical velocity, and what is the distance that the parcel overshoots its level of neutral buoyancy?

M9.4. The MATLAB script **lee_wave_1.m** uses the Fourier series approach to solve for flow over an isolated ridge for the case of constant N and constant mean zonal flow. For the case of $\bar{u} = 50$ m s^{-1}, run the script for various ridge widths to determine the width is required for significant vertical propagation (i.e., at what ridge width do phase lines of vertical velocity begin to tilt with height)?

M9.5. The script **lee_wave_2.m** plots an approximate analytic solution for flow over a mountain in the wide ridge limit. The height profile is given by

$$h(x) = h_0 L^2 \Big/ \left(L^2 + x^2 \right)$$

where L is the width scale of the ridge and h_0 is the ridge height. For a fixed ridge height of 2 km, vary the input zonal mean wind and comment on the dependence of the contoured solutions. (Note that the vertical scale is given in vertical wavelengths as in Figure 9.7.) Modify the script to vary the mountain height and determine what fraction of the vertical wavelength the mountain height must have in order for wave breaking to occur. (The onset of wave breaking occurs when the streamlines become vertical.)

M9.6. Consider stationary gravity waves forced by flow over a sinusoidal lower boundary for a case in which the static stability decreases rapidly with height at about the 6-km level. Thus, the buoyancy frequency is altitude dependent and the simple analytic solution (9.32) no longer applies. The MATLAB script named **linear_grav_wave_1.m** gives a highly accurate numerical solution for this situation.

(a) Describe the qualitative change in the wave behavior as the zonal wavelength is changed over the range of 10 to 100 km. Be sure to comment on momentum flux as well as on vertical velocity.

(b) Determine as accurately as you can what the minimum zonal wavelength is for vertical propagation to occur in the upper part of the domain (above the 6-km level).

(c) Determine how the amplitudes of the momentum flux and momentum flux convergence at $z = 6$ km change as the zonal wavelength is increased from 20 to 100 km. Do several different wavelengths so you can plot graphs of the dependence of the magnitudes of the momentum flux and zonal force on the wavelength of the sinusoidal topography. Use MATLAB to plot these two graphs.